ABSTRACT

Title of thesis: HEIGHT ESTIMATION AND CONTROL OF A ROTORCRAFT IN GROUND EFFECT USING MULTIPLE PRESSURE PROBES

Chin Gian Hooi, Master of Science, 2015

Thesis directed by: Dr. Derek A. Paley
Department of Aerospace Engineering

This thesis describes a dynamic height estimator and controller for rotorcraft landing and hovering in ground effect based on flowfield sensing and modeling. The rotor downwash in ground effect is represented using a ring-source potential flow model selected for real-time use. Experimental verification of the flow model and an augmented flow model for tilt are presented. A nonlinear dynamic model of a compound pendulum heave test stand that reduces to the dynamics of a rotorcraft in ground effect is presented with open-loop analysis and closed-loop control simulation. Equations of motion and stability characterization of of a heaving rotor IGE are derived for external perturbations and it is shown that a uniform sideward wind does not cause instability and uniform axial wind from the top can cause instability. Flowfield velocity measurements are assimilated into a grid-based recursive Bayesian filter to estimate height above ground in both simulation and experiment. Height tracking in ground effect and landing using the estimated height are implemented with a dynamic linear controller in both simulation and experiment. Mean estima-

tion and motion errors are found to be no greater than 5% and 9% respectively, demonstrating that height estimation and control is possible with only flow sensing and modeling.

HEIGHT ESTIMATION AND CONTROL OF A ROTORCRAFT IN GROUND EFFECT USING MULTIPLE PRESSURE PROBES

by

Chin Gian Hooi

Thesis submitted to the Faculty of the Graduate School of the
University of Maryland, College Park in partial fulfillment
of the requirements for the degree of
Master of Science
2015

Advisory Committee:
Dr. Derek A. Paley, Chair/Advisor
Dr. Anya R. Jones
Dr. Sean J. Humbert

Dedication

妈，我爱您！

“Essentially, all models are wrong, but some are useful.”

– George E.P. Box

Acknowledgments

妈和肥妹，谢谢您一路来的爱与鼓励。 To my friends and colleagues at the Collective Dynamics and Control Laboratory, it has been an eye-opening and humbling journey indeed. Prof. Derek Paley, thank you for your unparalled guidance and advice. Frank Lagor, your genius, patience and humor were second to none. William Craig and Dr. Derrick Yeo, thank you for your ideas, advice and assistance in building the heave test stand. Daigo Shishika, your math skills and logic were invaluable to my seeing the light at the end of the tunnel (luckily it was the exit!). Dr. Feitian Zhang, Nitin Sydney, Amanda Chicoli and Prof. Levi DeVries, thank you for the valuable discussions. I would also like to extend my warm gratitude to my committe members, Prof, Sean Humbert and Prof. Anya Jones for your valuable insight into my area of research.

A shoutout to Daria Long for your patience and (attempted) humor. To my friends and classmates, Alex Dean, Peter Rossonni, Jeff Gillette, Vera Klimchenko, Justine Li, Arthur Sakamoto, Ehsan Karim and the many others that I may have inevitably missed, thank you for your inquisitiveness and motivation. Minion Monica Hew, your research ideas and suggestions were indispensable to this being completed in time. A warm acknowledgement also has to be extended to the Aerospace Engineering Department staff who were immensely helpful in matters of administration and guidance, whom include Tom Hurst, Laura Thorsen and Lavita Williams. This work is supported by the University of Maryland Vertical Lift Rotorcraft Center of Excellence Army Grant No. W911W61120012.

Table of Contents

List of Figures

Chapter 1: Introduction

1.1 Introduction

Rotorcraft operation in ground effect (IGE) presents substantial challenges for vehicle control, including landing with low-impact velocity and maintaining near-ground hover in low-visibility conditions such as brownout [1], fog [2], snow or darkness. Safe operation IGE requires a controller capable of handling uncertainty. Previous authors have developed landing controllers based on robust or adaptive control techniques. For example, Serra and Cunha [3] adopt an affine parameter-dependent model that describes the helicopter linearized error dynamics for a predefined landing region and implements H_2 feedback control. Mahony and Hamel [4] develop a parametric adaptive controller that estimates the helicopter aerodynamics onboard and modulates the motor torque, rather than the collective pitch, during takeoff and landing and takes advantage of the reduced sensitivity of the control input to aerodynamics effects. Nonaka and Sugizaki [5] implement ground-effect compensation and integral sliding mode control to suppress the modeling error of the vehicle dynamics in ground effect. These control techniques often require a system model with empirically fit aerodynamic coefficients that are unique to each vehicle.

Safe operation IGE also requires accurate estimation of the proximity and

relative orientation of the ground plane. Height-estimation methods currently exist for micro aerial vehicles (MAVs) based on ultrasonic, barometric pressure or optical sensors. However, ultrasonic sensors work only for proximity sensing and do not work well for an angled or irregular ground plane [6]. Barometric pressure sensors typically work well for large height differentials [7], but are sensitive to fluctuations in atmospheric pressure, which results in sensor drift. Likewise, the effectiveness of vision-based sensors is limited in degraded visual environments and the algorithms used typically require great computational resources. This thesis develops a hover and landing controller that uses rotor downwash flow-velocity measurements and an aerodynamic model to estimate the height above ground, thereby providing an additional sensing modality for hovering and landing IGE.

Previous authors have quantified ground effect empirically or through the use of an underlying aerodynamic model. Nonaka and Sugizaki [5] take an empirical approach to measuring the ground effect on rotor thrust as a function of motor voltage. Mahony and Hamel [4] use an approximation of the down-flow velocity ratio based on a piecewise linear approximation of Prouty [8] to estimate rotor-thrust variation IGE. Higher fidelity analytical models include free vortex modeling [9] and other Computational Fluid Dynamics method, which seek to accurately predict the nature of the rotor wake vortices. Cheeseman and Bennett [10] provide a classic analytical model for ground effect, which I adopt for this work, based on aerodynamic modeling using the method of images. The use of an aerodynamic model permits comparison to measurements from sensors such as multi-component differential-pressure airspeed sensors [11]. Lagor et al. [12] and DeVries et al. [13]

have previously shown that a reduced-order flow model can be rapidly evaluated within a Bayesian filter to perform estimation and control tasks in an uncertain flow environment.

My previous paper [14] developed the theoretical framework for a dynamic controller for hover and landing IGE based on a flow model for height estimation. Rotorcraft downwash IGE was modeled using potential flow theory. I extended the model of Cheeseman and Bennett [10] using multiple ring sources; the mirror images create a ground plane. The reduced-order model relates the flowfield velocities to height IGE; it is capable of relatively fast evaluation for control purposes. A nonlinear dynamic model of rotorcraft landing IGE was presented, assuming a rigid rotor commonly found in MAV rotorcraft [15]. Height estimation of rotorcraft IGE using spatially distributed airspeed measurements was accomplished in simulation with a grid-based recursive Bayesian filter. The Bayesian framework is capable of fusing data from additional sensing modalities and for estimation of additional states, such as roll and pitch relative to the landing platform. The feedback controller was implemented in simulation to illustrate the theoretical results.

My following paper [16] outlined an improved ring-source potential flow model consistent with experimental observations. I derived a nonlinear dynamics model of a compound pendulum heave test stand that reduced to the dynamics of a rotorcraft IGE. Experimental results of the open-loop pendulum dynamics were detailed. I also presented experimental validation of the flow model and height estimation framework.

1.2 Motivation

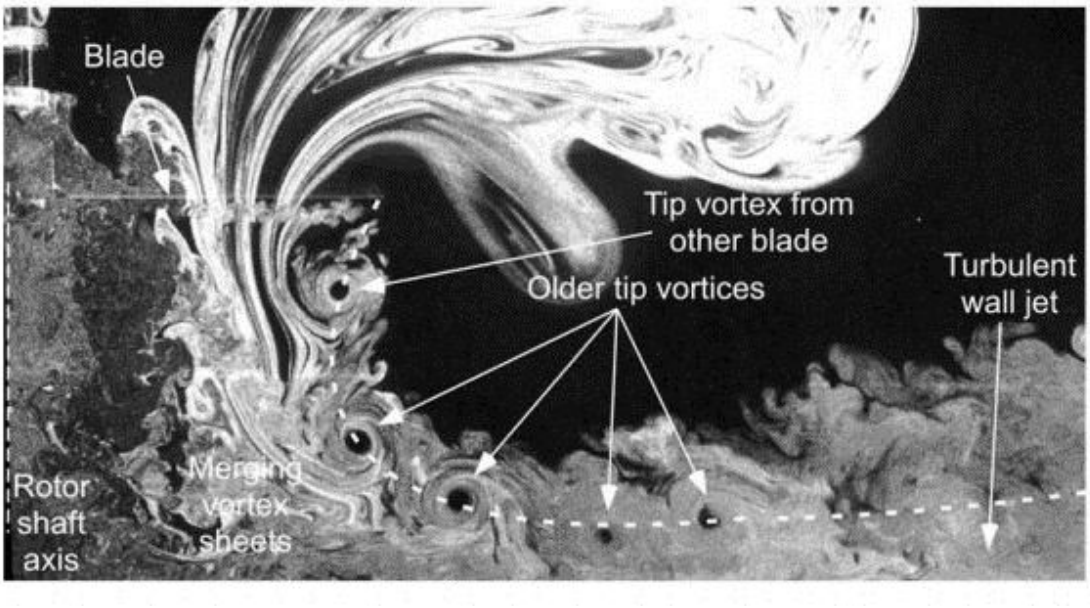

Figure 1.1: Flow visualization of rotor in Ground Effect [17].

Modeling the flowfield of a rotor IGE is a nontrivial task due to the complexity of the flowfield, as shown in Fig. 1.1 [17]. Many previous attempts at modeling have been made, as detailed above, but the main motivation for me as a control engineer is to develop a flow model that can be recursively evaluated in real-time within a high bandwidth control loop. Ideally, the estimation algorithms and control laws developed would also be computationally efficient. This framework would be useful for no-visibility altitude estimation using only flow sensors, with applications including autonomous shipboard landing.

This thesis proposes using reduced-order flow modeling to model the rotor flowfield IGE. Flow velocity components are measured using multi-component differential pressure probes [11] and compared with the flow model in a grid-based

recursive Bayesian filter to estimate rotorcraft height. Finally, an observer based closed-loop controller seeks to drive the vehicle to the commanded height.

1.3 Contributions

The contributions of this thesis are

1. A ring-source potential flow model for heave consistent with experimental observations and for roll or pitch. Previous potential flow models [10] are capable of predicting rotor performance IGE but do not predict the flowfield velocities well. Flowfield velocity components are crucial for height estimation IGE as they are directly measurable quantities. The ring-source potential flow model is capable of generating rotor flowfield velocity components and is also computationally efficient enough to be evaluated in real-time. The flow model is also augmented for roll or pitch for prediction of the flowfield velocities and streamlines of a tilting rotor.

2. Experimental validation of the ring-source potential flow model for heave. The flow model makes certain assumptions based on potential flow theory and only captures the mean velocity components. These assumptions are essential to the flow model predictions and have to be validated since previous potential flow models in literature have been lacking in flow velocity predictions. The velocity predictions are compared against experimental results for varying parameters. The comparisons validate the model, certify its parametric region of validity and illustrate the tradeoff between real-time efficiency and model fidelity.

3. A nonlinear dynamic model of a compound pendulum heave test stand. The dynamics of the heave stand is shown to reduce to the dynamics of a rotorcraft IGE with certain assumptions, demonstrating that the experimental setup mimics the system being studied, while being an effective setup. The dynamic model also allows for the study of the open-loop system dynamics and facilitates the design of a model-based closed-loop controller.

4. Equations of motion and stability characterization of of a heaving rotor IGE with external perturbations. It is shown that a uniform sideward wind does not cause instability of the rotor in ground effect, but rather increases its thrust. A uniform axial wind from the top of the rotor can cause instability, if it has greater magnitude than the induced velocity.

5. Experimental validation of the flow-sensing based height estimation and closed-loop height tracking framework. Experiments were conducted to validate the Bayesian filter height estimation framework with multiple differential pressure sensors measurements. Height estimation was found to be accurate to within 5% of the actual height. Subsequently, the estimated height was fedback for validation of the observer-based closed-loop height tracking controller, with height tracking accurate to within 9% of the desired height. It is shown that height estimation and tracking is possible using only flow sensing and modeling.

1.4 Thesis Outline

Chapter 2 describes the ring-source potential flow model representing a rotor flowfield IGE for both heave and roll or pitch. Chapter 3 derives the dynamics of a compound pendulum heave test stand and a rotorcraft operating IGE, with and without external perturbations. Chapter 4 details the prefiltering, Bayesian filter height estimation and speed estimation algorithms. Chapter 5 presents the control design of a Linear Quadratic Regulator and a Proportional Integral controller with feedfoward. Chapters 6 and 7 outline the experimental setup and validation for the flow model, height estimation and observer-based feedback control. Chapter 8 provides the conclusion to this thesis.

Chapter 2: Flow Model

2.1 Cheeseman and Bennett Potential Flow Model

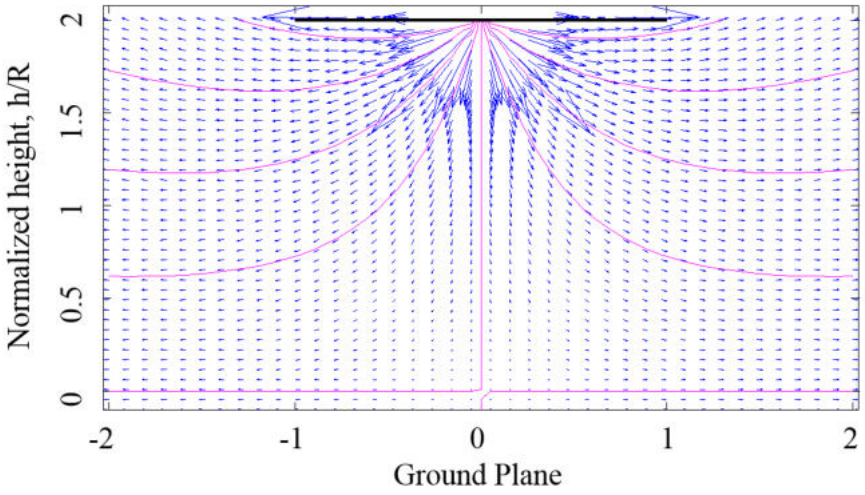

Figure 2.1: Cheeseman and Bennett [11] potential flow model of rotor downwash in ground effect.

Let R be the rotor radius, v_i denote the rotor induced velocity and h be the rotor height. Cheeseman and Bennett [10] model the rotor downwash IGE impinging on the ground plane by representing the rotor as a three-dimensional source with strength $s = R^2 v_i/4$ and the ground plane as a mirror-image source to enforce no flow through the ground plane, as shown in Fig. 2.1. The sources are separated by a distance $2h$.

The velocity potential for the location (x, y, z) in the flowfield is [10]

$$\phi = -\frac{s}{\sqrt{x^2 + y^2 + (z-h)^2}} - \frac{s}{\sqrt{x^2 + y^2 + (z+h)^2}}. \tag{2.1}$$

Taking the gradient of the velocity potential with respect to position yields the flow velocity components [10].

Although the Cheeseman and Bennett flow model has been experimentally shown to accurately capture the relationship between rotor thrust IGE and rotor height [10], it represents the physical flowfield of a rotor IGE with insufficient accuracy for my purposes. As shown in Fig. 2.1, the flow vectors just below the rotor plane extend radially outward as opposed to downward. Since the rotor is modeled as a point source, the strongest vectors are at the hub and diffuse in strength radially outward.

2.2 Ring-source Potential Flow Model

Similar to the Cheeseman and Bennett model, I model the physical flowfield using potential flow theory. However, I replace the single source of Cheeseman and Bennett with multiple ring sources to allow uniform spatial distribution of the flowfield sources.

As shown in Fig. 2.2, the rotor is modeled by N ring sources and the ground plane is modelled by their mirror images to enforce no flow through the ground plane. Note that ring $k = 1$ is at the rotor tip and the ring indices move radially

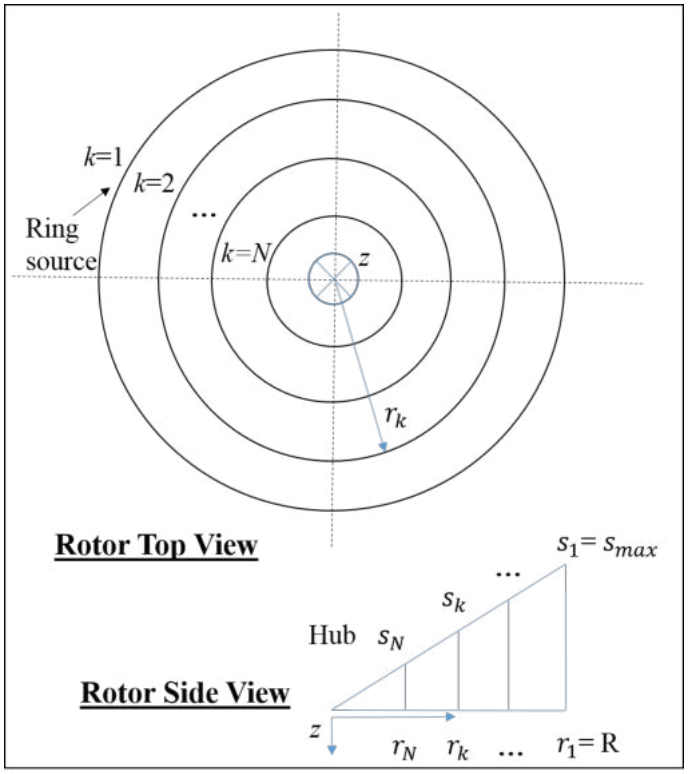

Figure 2.2: Schematic of ring-source potential flow model nomenclature.

inward with equal radial spacing of R/N. The radial location of each ring k is

$$r_k = R - (k-1)\frac{R}{N}. \tag{2.2}$$

Similar to the inflow ratio distribution of a rotor [18], the strength s_k of ring k varies with radial location according to

$$s_k = \frac{s_{max}}{R} r_k, \tag{2.3}$$

where the maximum source strength s_{max} is located at the rotor tip $r_1 = R$. I choose the source strengths according to the total volumetric flow through the rotor disk, similar to Cheeseman and Bennett. Let $A = \pi R^2$ denote the rotor disk area. The

strength of each ring source s_k represents the volumetric flow rate per unit length and the total flow rate satisfies

$$\frac{1}{2}\sum_{k=1}^{N} 2\pi r_k s_k - \frac{1}{4}(2\pi R s_{max}) = A v_i. \tag{2.4}$$

Although the ring sources emanate in all directions, only the bottom half of the emanation should be modeled as the rotor flow. Additionally, the outer most ring source, which happens to be the strongest, should only have a quarter of its emanation considered because the emanation outwards and upwards do not contribute to the rotor flow. From arithmetic series and sum of a sequence of squares,

$$\sum_{k=1}^{N} k = \frac{N(N+1)}{2} \quad \text{and} \quad \sum_{k=1}^{N} k^2 = \frac{N(N+1)(2N+1)}{6}. \tag{2.5}$$

Substituting (2.2), (2.3) and (2.5) into (2.4) yields

$$s_{max} = \frac{6NRv_i}{2N^2+1}. \tag{2.6}$$

The velocity potential of ring source k is [19]

$$\phi_k(r, r_k, z) = \frac{-s_k r_k K(M)}{\pi\sqrt{\rho_1(r, r_k, z)}}, \tag{2.7}$$

where $\rho_1 = (r + r_k)^2 + z^2$, r and z are the radial location and elevation of the query point in the rotor body frame (positive down), respectively, and $M = 4rr_k/\rho_1$. The

radial $v_k(\rho_1, \rho_2)$ and vertical $w_k(\rho_1, \rho_2)$ velocity components of ring source k are [19]

$$v_k = \frac{r_k s_k}{2\pi r\sqrt{\rho_1}}\left[K(M) + \frac{r^2 - r_k^2 - z^2}{\rho_2}E(M)\right] \tag{2.8}$$

$$\text{and} \quad w_k = \frac{-s_k r_k z E(M)}{\pi\rho_2\sqrt{\rho_1}}, \tag{2.9}$$

where $\rho_2 = (r - r_k)^2 + z^2$ and $K(M)$ and $E(M)$ are the first and second complete elliptic integrals respectively ($K(M)$ and $E(M)$ are evaluated using the `ellipke` function in MATLAB). The velocity components of the flowfield are the sum of each ring source and their image ring-source contributions, i.e.,

$$v(r, z) = \sum_{k=1}^{N} v_k(\rho_1, \rho_2) + \sum_{k=1}^{N} v_k(\bar{\rho_1}, \bar{\rho_2}), \tag{2.10}$$

$$w(r, z) = \sum_{k=1}^{N} w_k(\rho_1, \rho_2) + \sum_{k=1}^{N} w_k(\bar{\rho_1}, \bar{\rho_2}), \tag{2.11}$$

where $\bar{\rho_1} = (r + r_k)^2 + (2h - z)^2$ and $\bar{\rho_2} = (r - r_k)^2 + (2h - z)^2$.

Fig. 2.3 shows the flowfield generated by the ring-source potential flow model, with streamlines and speed distribution shown for various heights. Speed is denoted by $\|V\| = \sqrt{v^2 + w^2}$. The variations in speed distribution with height serve as an informative tool for the placement of sensors to measure the flowfield experimentally. The potential flow model is qualitatively similar to the flow visualization model of the flowfield below a rotor IGE by Lee et al. [17], as shown by Fig. 2.4.

Moving from the rotor plane to the ground close to the rotor hub, the flow decelerates and forms a stagnation region. Moving radially outward, the flow deceleration region is easiest to distinguish for h=1.0R in Fig. 2.3 from the light blue

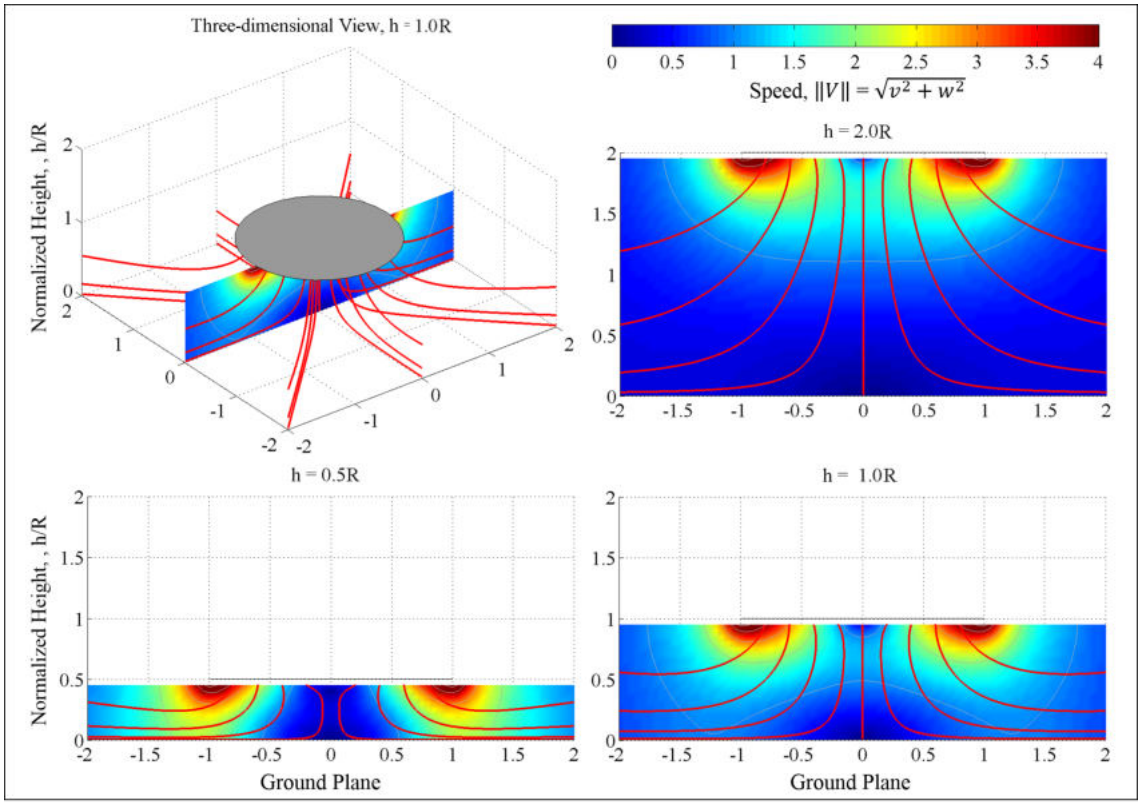

Figure 2.3: Flowfield of ring-source potential flow model evaluated at various heights, depicting streamlines and speed distributions, where speed $\|V\| = \sqrt{v^2 + w^2}$.

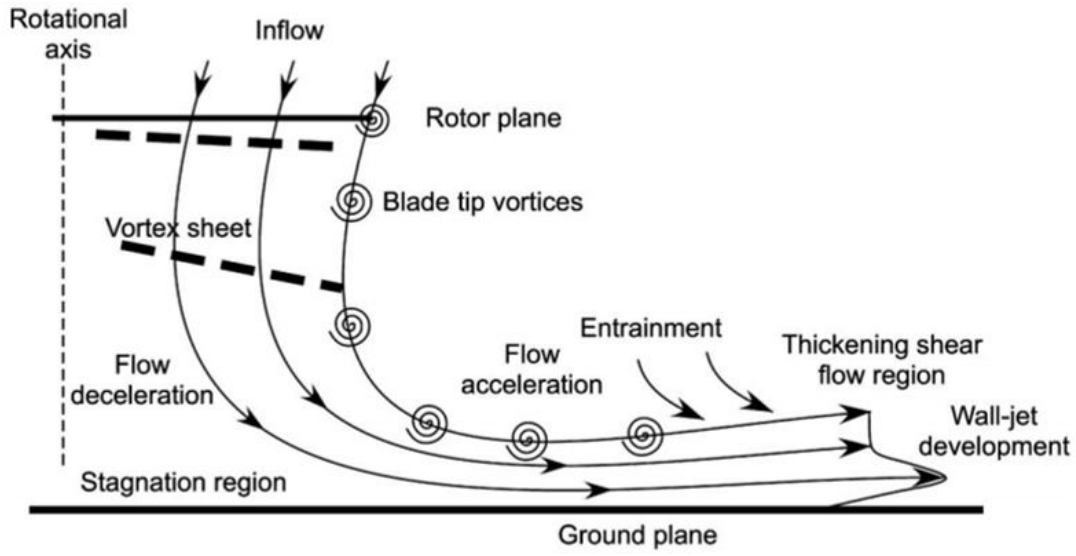

Figure 2.4: General developments of rotor flowfield in Ground Effect [17]

color map. In contrast, the flow acceleration region is where the streamlines change direction from pointing downward to pointing radially outward. As the rotor approaches the ground, the streamlines are compressed, which is best illustrated for h=0.5R in Fig. 2.3. Evidently, the flow speed is the highest in the flow acceleration region for the h=0.5R case as opposed to the h=2.0R case, since the flow is being compressed more with less space between the rotor plane and the ground. This effect is analogous to moving a water jet (the rotor) closer to a wall (the ground plane), since the jet speed in the flow acceleration region is highest when it is close to the wall.

Although the rotor downwash IGE as visualized in the work of Lee et al. [17] is not laminar, I model it using potential flow theory and account for turbulence with process noise (see Height and Speed Estimation Section). I model the mean velocity of the dominant flow and treat the turbulence and other secondary effects, such as blade tip vortices, as fluctuations away from the mean. Flow velocity component measurements $\tilde{V}$ are collected below the rotor in the experimental setup. Airspeed measurements of the sort described in [11] contain two flow velocity components, radial $\tilde{v}$ and vertical $\tilde{w}$, at each airspeed probe set location and are collected in an array configuration to sample the flowfield at multiple spatial locations. In reality, differential pressure is measured and converted into airspeed, so it is more accurate to call them differential pressure probes. Measurement $\tilde{V}$ corresponds to either the radial $\tilde{v}$ or the vertical $\tilde{w}$ velocity component. I assume the velocity component V is corrupted by zero-mean Gaussian white noise η with standard deviation σ_η and

zero mean, resulting in the measurement model

$$\tilde{V} = V + \eta. \tag{2.12}$$

2.3 Ring-source Potential Flow Model with Tilt

The ring-source potential flow model can be augmented to generate the flow-field of a rotor with a roll or pitch angle relative to a horizontal ground plane. Since it's easier to work in Cartesian coordinates for tilt, I convert the radial location of the query point r (in rotor body frame $\mathbb{A}$) to x and y as follows

$$x = r\cos\gamma, \quad y = r\sin\gamma, \tag{2.13}$$

where γ is the angle from the positive rotor body frame $\hat{a}_x$-axis to r as shown in Fig. 2.5. Note that the ring-source is mirrored by its image source about the horizontal ground plane such that a rotor roll or pitch angle θ is introduced. The rotation matrix from inertial frame $\mathbb{I}$ to rotor body frame $\mathbb{A}$ is

$${}^{A}R^{I} = \begin{bmatrix} \cos\theta & 0 & -\sin\theta \\ 0 & 1 & 0 \\ \sin\theta & 0 & \cos\theta \end{bmatrix}, \tag{2.14}$$

where θ is the roll or pitch angle relative to the horizontal ground plane.

Evaluation of the velocity components with rotor tilt is similar to the heave

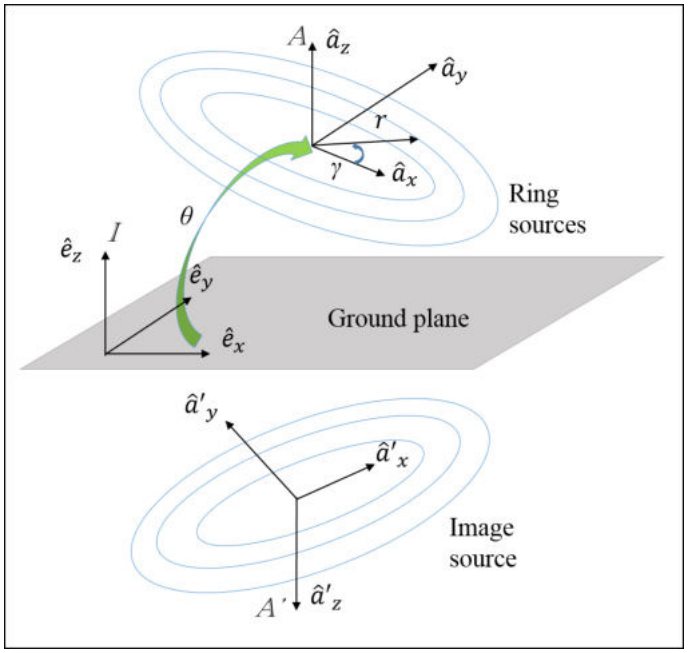

Figure 2.5: Schematic of nomeclature for ring-source potential flow model with tilt.

case but with some subtle differences. I evaluate the velocity components of the ring source and its image separately in their body frames respectively. The velocity components of the ring source in its body frame $\mathbb{A}$ is

$$ {}^{A}u_\theta(x,y,z) = \cos\gamma \sum_{k=1}^{N} v_k(\rho_1,\rho_2), \tag{2.15} $$

$$ {}^{A}v_\theta(x,y,z) = \sin\gamma \sum_{k=1}^{N} v_k(\rho_1,\rho_2), \tag{2.16} $$

$$ {}^{A}w_\theta(x,y,z) = \sum_{k=1}^{N} w_k(\rho_1,\rho_2). \tag{2.17} $$

The rotation matrix from inertial frame $\mathbb{I}$ to image source body frame $\mathbb{A}'$ is

$$ {}^{A'}R^{I} = \begin{bmatrix} -\cos\theta & 0 & -\sin\theta \\ 0 & 1 & 0 \\ \sin\theta & 0 & -\cos\theta \end{bmatrix}. \tag{2.18} $$

Location of the query point in the image body frame $\mathbb{A}'$ is

$$ \begin{bmatrix} x \\ y \\ z \end{bmatrix}_{A'} = {}^{A'}R^{I} \begin{bmatrix} x \\ y \\ 2h - z \end{bmatrix}. \tag{2.19} $$

The velocity components of the image in the image body frame ${}^{A'}u_\theta, {}^{A'}v_\theta, {}^{A'}w_\theta$ are evaluated using the coordinates (2.19) in (2.15), (2.16) and (2.17). Finally, the velocity components of the flowfield in the inertial frame $\mathbb{I}$ are the sum of the rotated source and image velocity components,

$$ \begin{bmatrix} {}^{I}u_\theta \\ {}^{I}v_\theta \\ {}^{I}w_\theta \end{bmatrix} = {}^{I}R^{A} \begin{bmatrix} {}^{A}u_\theta \\ {}^{A}v_\theta \\ {}^{A}w_\theta \end{bmatrix} + {}^{I}R^{A'} \begin{bmatrix} {}^{A'}u_\theta \\ {}^{A'}v_\theta \\ {}^{A'}w_\theta \end{bmatrix}. \tag{2.20} $$

The rotation matrices from body to inertial frames are ${}^{I}R^{A} = ({}^{A}R^{I})^{T}$ and ${}^{I}R^{A'} = ({}^{A'}R^{I})^{T}$.

Fig. 2.6 shows the flowfield of ring-source potential model (2.20) with prescribed motion of varying tilt angles. The illustration shows the streamlines being

compressed on the side that the rotor tilts towards the ground. On the tilting side, the corresponding speed $\|V\| = \sqrt{{}^{I}u_{\theta}^{2} + {}^{I}v_{\theta}^{2} + {}^{I}w_{\theta}^{2}}$ is relatively higher as shown by the fifty shades of blue. The flow model allows the tilt of the rotor relative to a horizontal ground plane and is useful for estimation of roll or pitch angle.

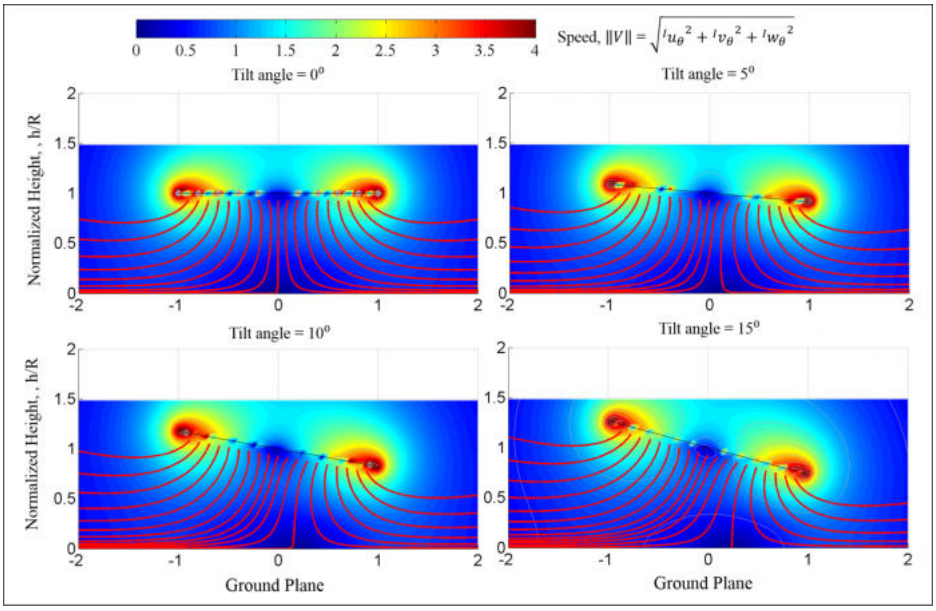

Figure 2.6: Flowfield of ring-source potential model with prescribed motion of varying tilt angle, showing streamlines and speed where speed $\|V\| = \sqrt{{}^{I}u_{\theta}^{2} + {}^{I}v_{\theta}^{2} + {}^{I}w_{\theta}^{2}}$.

Chapter 3: Dynamics

3.1 Dynamics of a Compound Pendulum Heave Test Stand

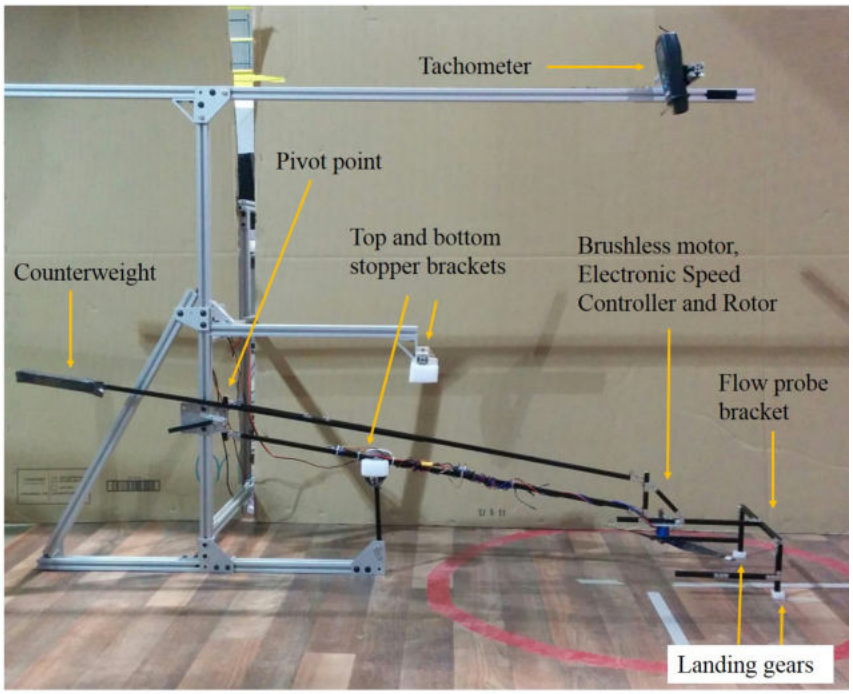

Figure 3.1: Compound pendulum heave test stand.

Two heave test stands were built for experimental verification of the flow-sensing and control framework, one static and another dynamic. Fig. 3.1 shows the compound pendulum heave test stand used to verify the flow model, dynamics and closed-loop control. The compound pendulum test stand is constructed as a parallelogram setup so that the rotor is always parallel to the ground plane with

one degree of freedom in the heave direction. This setup allows the use of journal bearings, which are smoother than linear carriages and rails in a vertical configuration for my static test setup. This setup also has the added benefit of allowing a counterweight to balance the system weight and to reduce the motor load.

Fig. 3.2 shows the free-body diagram of the compound pendulum. The lateral ($\hat{e}_y$) displacement can be minimized by mounting the setup at the midstroke, i.e., at a height of $1.25R$.

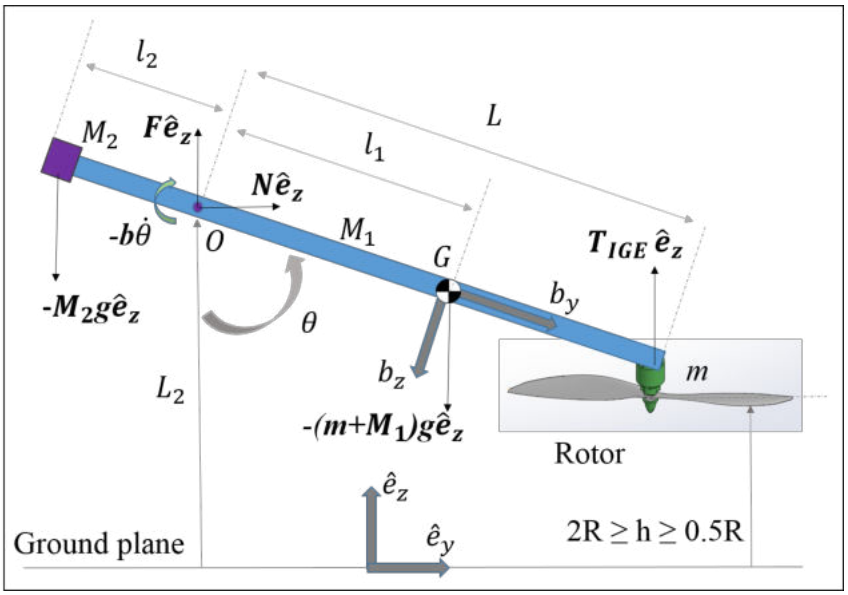

Figure 3.2: Free body diagram of compound pendulum heave test stand.

3.1.1 Dynamics

The angular momentum of the compound pendulum is

$$h_o = I_o \dot{\theta} e_x, \tag{3.1}$$

where I_o is the moment of inertia about point O, θ is the positive clockwise angle from vertical and $\dot{\theta}$ is the angular velocity of the pendulum. The time derivative of the angular momentum equals the moment about point O. In the $\hat{e}_x$ direction,

$$I_o\ddot{\theta} = LT_{IGE}\sin\theta - l_1 g\sin\theta(m + M_1) + l_2 M_2 g\sin\theta - b_2\dot{\theta}, \tag{3.2}$$

where $\ddot{\theta}$ is the angular acceleration; l_1, l_2 and L are the distances from O to the center of mass, O to counterweight M_2 and O to rotor mass m respectively; M_1 is the mass of the pendulum setup and b_2 is the damping coefficient due to aerodynamics and/ or friction. Table 3.1 shows these parameter values for my setup.

Table 3.1: Parameter values for compound pendulum heave test stand with rotor radius $R = 0.1778$ m (7 in).

Parameter	l_1	l_2	L	m	M_1	M_2
Value	0.2921 m (11.5 in)	0.4572 m (18 in)	0.9398 m (37 in)	0.35 kg (0.7714 lb)	0.304 kg (0.6702 lb)	0.34 kg (0.7496 lb)

The rotor thrust is augmented for ground effect T_{IGE} using the Cheeseman and Bennett model [10], which captures the essential characteristic of the relationship between thrust T and height IGE, i.e.,

$$T_{IGE} = \frac{1}{1 - \frac{R^2}{16h^2}}T = \frac{16h^2}{16h^2 - R^2}T. \tag{3.3}$$

Based on experimental data, Leishman [18] suggests that model (3.3) is valid for 2.0 $\geq h/R \geq$0.5.

In terms of the height $h = L_2 - L\cos\theta$,

$$\dot{h} = L\dot{\theta}\sin\theta, \tag{3.4}$$

$$\ddot{h} = L\dot{\theta}^2\cos\theta + L\ddot{\theta}\sin\theta. \tag{3.5}$$

Since the compound pendulum is mounted at midstroke, I approximate $\theta \approx \pi/2$, which implies

$$h \approx L_2, \quad \dot{h} \approx L\dot{\theta} \quad \text{and} \quad \ddot{h} \approx L\ddot{\theta}. \tag{3.6}$$

Likewise, the moment of inertia I_o is

$$I_o = mL^2 + \frac{1}{3}M_1(L + l_2)^2 + M_2{l_2}^2. \tag{3.7}$$

Substituting (3.3) and (3.6) into (3.2) yields the dynamics of the compound pendulum heave test stand,

$$\ddot{h} = \frac{1}{I_o}\left[\frac{16h^2TL^2}{(16h^2 - R^2)} - l_1Lg(m + M_1) + l_2LgM_2\right] - b\dot{h}, \tag{3.8}$$

where $b = b_2/I_o$. Note that as the mass of the compound pendulum setup M_1 and the counterweight M_2 go to zero, i.e. if I ignore the mass of the support structure, the compound pendulum dynamics (3.8) reduce to the rotorcraft IGE dynamics (3.16).

3.1.2 Linear State Space Form

The state vector $Z \in \mathbb{R}^2$ is defined as

$$Z = \begin{bmatrix} h \\ \\ \dot{h} \end{bmatrix} = \begin{bmatrix} z_1 \\ \\ z_2 \end{bmatrix}, \tag{3.9}$$

where $\dot{h}$ is the landing speed. I define the control input for the compound pendulum heave test stand as

$$\nu_1 = T, \tag{3.10}$$

where T is the thrust out of ground effect. Note that the control input for the heave test stand ν_1 is defined slightly differently than the control input for the rotorcraft ν_2 (3.17).

The nonlinear state space form is

$$\dot{Z} = \begin{bmatrix} \dot{h} \\ \\ \ddot{h} \end{bmatrix} = \begin{bmatrix} z_2 \\ \\ \frac{1}{I_o}\left(\frac{16h^2TL^2}{(16h^2-R^2)} - l_1Lg(m+M_1) + l_2LgM_2\right) - b\dot{h} \end{bmatrix}. \tag{3.11}$$

The Jacobians

$$A = \begin{bmatrix} 0 & 1 \\ \\ \frac{-2gR^2}{z_1^*(16z_1^{*2}-R^2)} & 0 \end{bmatrix} \quad \text{and} \quad B = \begin{bmatrix} 0 \\ \\ \frac{16z_1^{*2}}{16z_1^{*2}-R^2} \end{bmatrix} \tag{3.12}$$

are the partial derivatives of the right-hand side of (3.11) with respect to Z and ν_1,

respectively. The linear system dynamics are

$$\dot{Z} = AZ + B\nu_1. \tag{3.13}$$

3.2 Dynamics of Rotorcraft Operation IGE

3.2.1 Dynamics

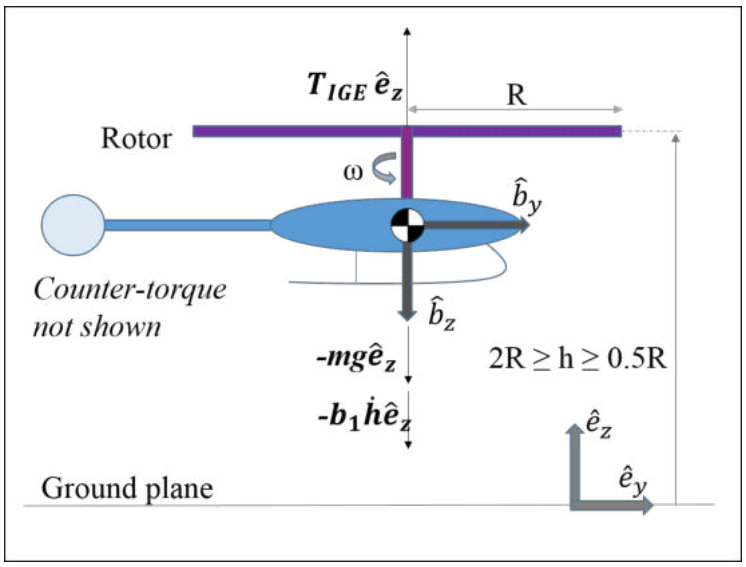

Figure 3.3: Free-body diagram of rotorcraft in ground effect.

Fig. 3.3 shows the free-body diagram of a rotorcraft in which the tail rotor counter-torque is not shown. Applying Newton's second law in the $\hat{e}_z$ direction yields

$$m\ddot{h} = T_{IGE} - mg - b_1\dot{h}, \tag{3.14}$$

where T_{IGE} is the rotor thrust IGE, m is the mass of the rotor, $\dot{h}$ and $\ddot{h}$ are the

vertical velocity and acceleration respectively, g is the gravitational acceleration and b_1 is the damping coefficient due to aerodynamics or another source. Modeling the rotor thrust T as a function of rotor rotational speed ω yields [15]

$$T = k\omega^2. \tag{3.15}$$

It is assumed henceforth that the rotorcraft has landed when h/R =0.5, which is reasonable since the rotor distance above the landing gear is typically greater than $0.5R$. Thrust IGE (3.3) is substituted into (3.14) to obtain the dynamics of a rotorcraft IGE,

$$\ddot{h} = \frac{16h^2 k\omega^2}{(16h^2 - R^2)m} - g - b_1\dot{h}. \tag{3.16}$$

3.2.2 Linear State Space Form

For the rotorcraft operating IGE, I define the control input as

$$\nu_2 = \frac{k\omega^2}{m}. \tag{3.17}$$

The nonlinear state space form is

$$\dot{Z} = \begin{bmatrix} \dot{h} \\ \ddot{h} \end{bmatrix} = \begin{bmatrix} z_2 \\ \frac{16z_1^2}{16z_1^2 - R^2}\nu_2 - g \end{bmatrix}. \tag{3.18}$$

An equilibrium control input ν_2^* is necessary to keep the rotorcraft hovering at

a corresponding equilibrium height z_1^* (or to land safely). Solving (3.25) for the equilibrium condition, $\dot{Z}^* = 0$, the equilibrium control input is

$$\nu_2^* = g\frac{16z_1^{*2} - R^2}{16z_1^{*2}}. \tag{3.19}$$

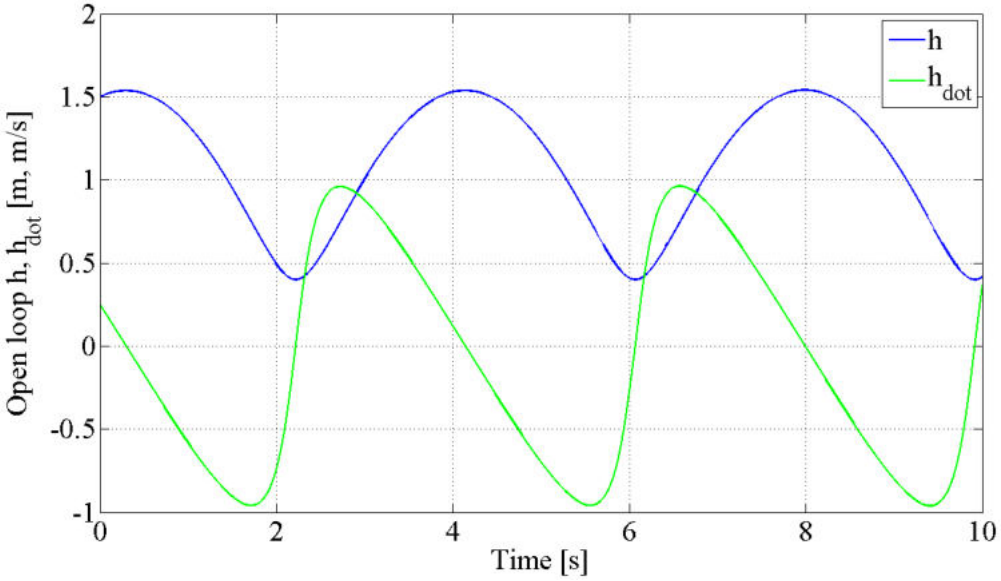

Figure 3.4: Open-loop dynamics of rotorcraft without damping in ground effect with constant input $\nu_2 = \nu_2^*$. Initial conditions for height and speed are (1.5m, 0.25m/s).

Fig. 3.4 depicts the simulation results of the open-loop nonlinear dynamics without damping for initial height and speed (1.5m and 0.25m/s) and constant input $\nu_2 = \nu_2^*$. In order to implement a linear controller for the nonlinear dynamics (3.25), the Jacobian matrices are needed. The Jacobians are

$$A = \begin{bmatrix} 0 & 1 \\ \frac{-2gR^2}{z_1^*(16z_1^{*2}-R^2)} & 0 \end{bmatrix} \quad \text{and} \quad B = \begin{bmatrix} 0 \\ \frac{16z_1^{*2}}{16z_1^{*2}-R^2} \end{bmatrix}. \tag{3.20}$$

3.3 Dynamics of Rotor IGE with Sideways and Axial Perturbation

Micro-rotorcraft are known to exhibit difficulties in flight when they encounter perturbations such as gusts or even flight under an air-condtioning duct. This phenomenon is exacerbated during applications such as shipboard landing when even small perturbations of a rotorcraft in ground effect can have disastrous effects, let alone micro-rotorcraft. The section derives the equations of motion and characterizes the stability of a heaving rotor IGE under external perturbation.

3.3.1 Sideways Perturbation

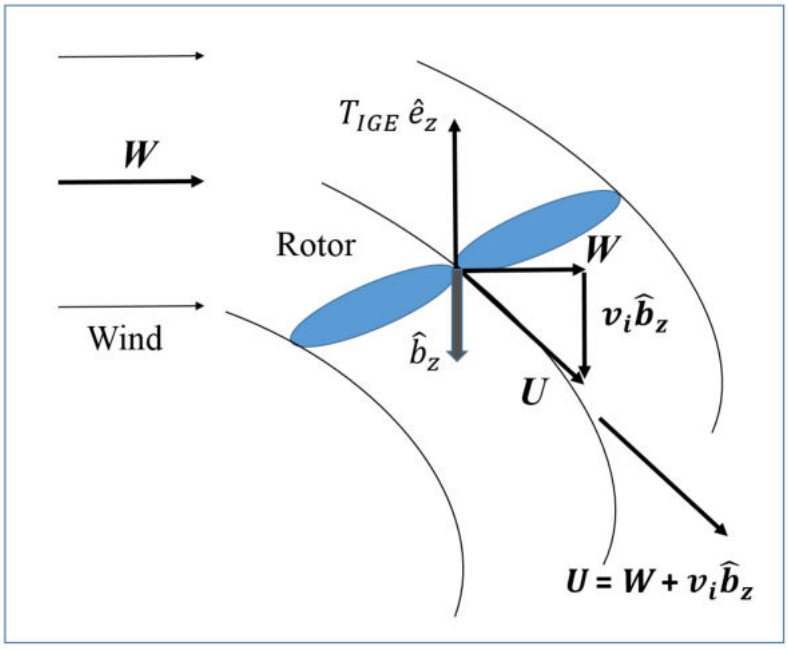

Figure 3.5: Control volume of rotor with perturbance $\boldsymbol{W}$ for momentum theory analysis.

In order to account for the change in the surrounding environment due to wind, I need a new expression for thrust. Bangura et. al [20] propose using momentum

theory analysis on a control volume shown in Fig. 3.5, such that thrust is [20]

$$T = 2\rho A v_i U, \tag{3.21}$$

where ρ is air density, $A = \pi R^2$ is the rotor disk area and v_i is the rotor induced velocity. $U = |\boldsymbol{U}|$ is the normed resultant velocity of the air through the rotor given by [20]

$$U = \sqrt{u^2 + v^2 + (v_i - w)^2}, \tag{3.22}$$

where u, v and w are the velocity components in the $\hat{b}_x, \hat{b}_y$ and $\hat{b}_z$ direction respectively.

Now assume a uniform sideward wind $v = |\boldsymbol{W}|$ impinges on the rotor. The rotor thrust due to this sideward wind is given by (3.21)

$$T = 2\rho A v_i \sqrt{v^2 + v_i^2}. \tag{3.23}$$

The dynamics (3.16) then become

$$\ddot{h} = \frac{32\rho A h^2}{(16h^2 - R^2)m} v_i \sqrt{v^2 + v_i^2} - g - \frac{b}{m}\dot{h},. \tag{3.24}$$

The nonlinear state space form is

$$\dot{Z} = \begin{bmatrix} \dot{h} \\ \\ \ddot{h} \end{bmatrix} = \begin{bmatrix} z_2 \\ \\ \frac{32\rho A z_1^2}{(16z_1^2 - R^2)m} V - g - \frac{b}{m} z_2 \end{bmatrix}, \tag{3.25}$$

where $V = \left(v_i \sqrt{v^2 + v_i^2} \right)$ for the sideward wind v case. The Jacobian

$$A = \begin{bmatrix} 0 & 1 \\ \\ a_{21} & -\frac{b}{m} \\ \\ \end{bmatrix} \tag{3.26}$$

is the partial derivative of the right-hand side of (3.25) with respect to Z about the hover equilibrium, $Z^* = [z_1^*, 0]^T$, where

$$a_{21} = \frac{-64\pi\rho R^4 z_1^* \left(v_i \sqrt{v^2 + v_i^2} \right)}{m(16 z_1^{*2} - R^2)^2}. \tag{3.27}$$

In order to characterize the stability of the rotor perturbed by a sideward wind v, consider the eigenvalue of A

$$\lambda = -\frac{b}{2m} \pm \frac{1}{2} \sqrt{(\frac{b}{m})^2 - \frac{256\pi\rho R^4 z_1^* \left(v_i \sqrt{v^2 + v_i^2} \right)}{m(16 z_1^{*2} - R^2)^2}}. \tag{3.28}$$

Since only a positive real eigenvalue will cause instability, I only focus on the positive square root part of the characteristic equation. In order to further simplify the eigenvalue, consider the boundary conditions for ground effect, i.e. $z_1^* = R/2$

and $2R$. For $z_1^* = R/2$, the eigenvalue of interest is

$$\lambda = -\frac{b}{2m} + \sqrt{(\frac{b}{2m})^2 - \frac{11.17\rho R}{m}\left(v_i\sqrt{v^2 + v_i^2}\right)}. \tag{3.29}$$

Since the square-root term is always smaller than $\frac{b}{2m}$, the eigenvalue is always negative and hence the system is stable for the boundary condition of $z_1^* = R/2$, where ground effect is the strongest. For the case of $z_1^* = 2R$, similar steps are taken as before such that (3.29) is then

$$\lambda = -\frac{b}{2m} + \sqrt{(\frac{b}{2m})^2 - \frac{0.1013\rho R}{m}\left(v_i\sqrt{v^2 + v_i^2}\right)}. \tag{3.30}$$

Similarly, the square-root term is always smaller than $\frac{b}{2m}$, hence the eigenvalue is always negative and the system is stable for $z_1^* = R/2$, where ground effect is the weakest. Hence, the rotor being perturbed IGE by a with sideward wind v is stable. Physically, (3.23) means that the rotor generates more thrust due to the sideward wind v and is referred to in the literature as *translational lift* [18].

3.3.2 Axial Perturbation

Now assume that an axial wind $w = |\boldsymbol{W}|$ impinges on the rotor from the top. I follow a similar procedure as the analysis of the sideward wind to characterize the stability. The rotor thrust caused by the wind is

$$T = 2\rho A v_i(v_i - w). \tag{3.31}$$

The dynamics of a rotor IGE under the influence of uniform axial wind w is

$$\ddot{h} = \frac{32\rho A h^2}{(16h^2 - R^2)m} v_i(v_i - w) - g - \frac{b}{m}\dot{h},. \tag{3.32}$$

Note that a few sources in the literature including [21] and [22] do *not* include the damping or drag term b into the heave dynamics but only do so for the translational dynamics. The reason cited was that the classical drag model predicts significant residual drag in hover [21]. Instead, Bangura and Mahony [21] (simplified even further by Leishman et. al. [22]) only include a simplified drag term on the translational dynamics.

My previous work [14] simulated the rotor heave dynamics IGE without damping with open-loop constant input, as shown in Fig. 3.4. This system represents a spring-mass system that constantly oscillates, but experimental observations dictate that these oscillations damp out pretty quickly, both due to drag and also friction from the connection points of a heave test stand. Also, without damping, the real parts of the system eigenvalues are zero, as is evident by setting $b = 0$ in (3.26), hence rendering the system stability inconclusive, which is not the case. As such, I proceed with the assumption that b is a positive constant.

The nonlinear state space form (3.25) has

$$V = v_i(v_i - w), \tag{3.33}$$

and a_{21} (3.34) in the the Jacobian (3.26) is

$$a_{21} = \frac{-64\pi\rho R^4 z_1^* \left(v_i(v_i - w)\right)}{m(16z_1^{*2} - R^2)^2}. \tag{3.34}$$

Similarly, the eigenvalue of the system which may cause instability is associated with the positive square-root term as in (3.28). Looking at the boundary condition $z_1^* = R/2$, the eigenvalue of interest is

$$\lambda = -\frac{b}{2m} + \sqrt{(\frac{b}{2m})^2 - \frac{11.17\rho R}{m}v_i^2 + \frac{11.17\rho R}{m}v_i w}. \tag{3.35}$$

If $v_i >> w$, the v_i^2 term within the square root dominates and I have a stable system. However, if $w >> v_i$, the w term dominates and (3.35) becomes

$$\lambda = -\frac{b}{2m} + \sqrt{(\frac{b}{2m})^2 + \frac{11.17\rho R}{m}v_i w}. \tag{3.36}$$

The square-root term for this case is larger than $\frac{b}{2m}$ and as such, the real part of the eigenvalue becomes positive for $w >> v_i$, which means the system is unstable!

The same argument can be made for the $z_1^* = 2R$ case, where the eigenvalue of interest is

$$\lambda = -\frac{b}{2m} + \sqrt{(\frac{b}{2m})^2 - \frac{0.1013\rho R}{m}v_i^2 + \frac{0.1013\rho R}{m}v_i w}. \tag{3.37}$$

Similar to the previous case, we have a stable system if $v_i >> w$, but if $w >> v_i$,

the w term dominates, (3.37) becomes

$$\lambda = -\frac{b}{2m} + \sqrt{(\frac{b}{2m})^2 + \frac{0.1013\rho R}{m} v_i w}, \tag{3.38}$$

and I have an unstable system.

If I examine (3.31), it is obvious that when $v = w$, the rotor stops producing thrust! This phenomenon is the onset of instability, since the system is perturbed far away from the equilibrium condition of hover it was linearized about and has no means of returning to the equilibrium point without thrust. If $w >> v_i$, the rotor then produces *negative thrust*. Physically, as the wind passes through the rotor, which has a constant speed regulated by a motor, the wind speed increases due to this additional power from the rotor and generates thrust, albeit antiparallel to the initial direction of rotor thrust. In essence, the wind is extracting power away from the rotor and if $w >> v_i$, all the thrust is generated by the wind in the opposite direction of the original rotor thrust.

Figs. 3.6(a), (b), (c) and (d) show the phase portraits of (3.32) with increasing vertical wind w magnitude. Fig. 3.6(a) shows a center (equilibrium point) at (z_1^*, z_2^*) = (0.7, 0), which is the equilibrium condition for v_i = 4m/s. Note that the lower limit of the horizontal axes is $z_1 = 0.25$ because this is the point at which the denominator for (3.3) goes to zero and the model breaks down. Fig. 3.6(b) shows the equilibrium point moving towards $z_1 = 0.25$ as w increases. Fig. 3.6(c) is when thrust is equal to zero, so the first term in (3.32) goes to zero. This is the onset of bifurcation as the equilibrium point has vanished and the system transitions into

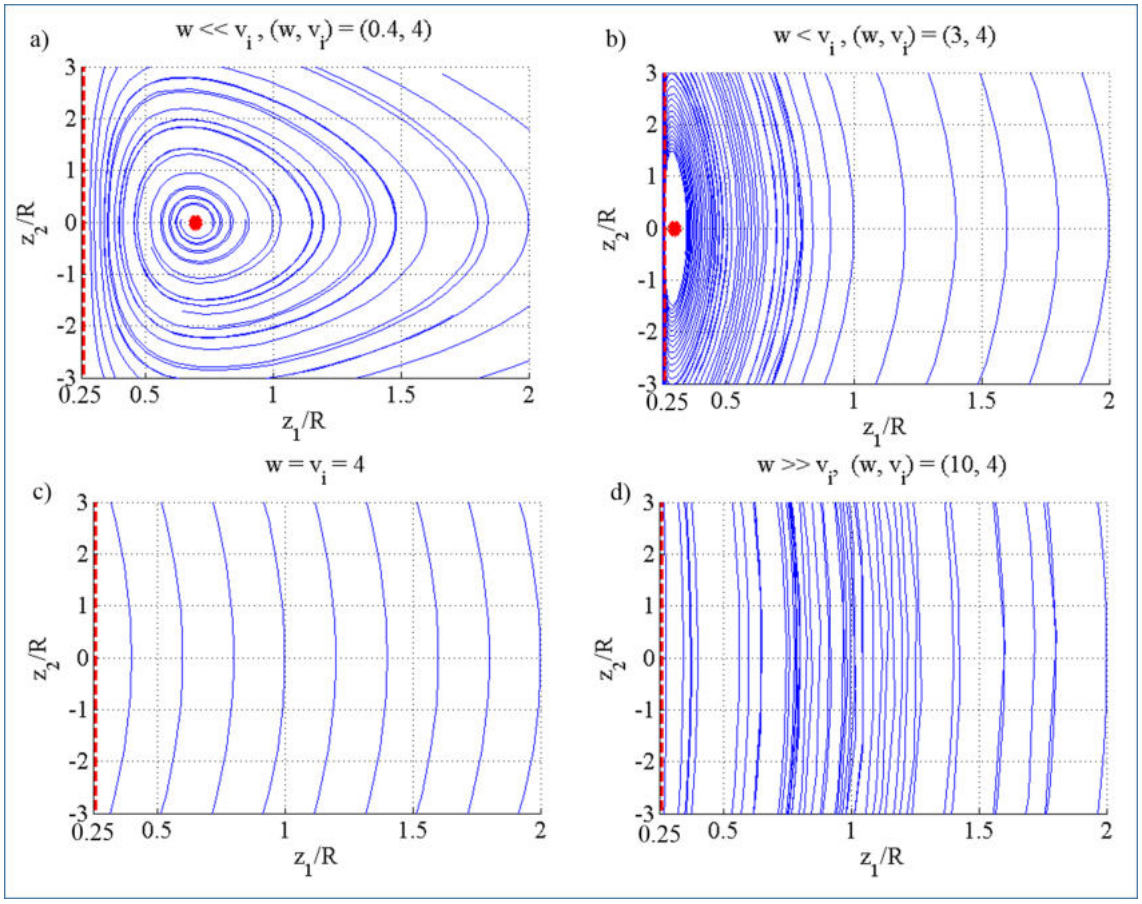

Figure 3.6: Open-loop dynamics of rotorcraft without damping in ground effect with constant input $\nu_2 = \nu_2^*$. Initial conditions for height and speed are (1.5m, 0.25m/s).

being unstable (from previously being stable). Fig. 3.6(d) shows the phase portrait of the unstable system, where again there are no equilibrium points.

Finally, as axial wind comes from below the rotor, it is akin to the rotor flow in descending flight, which enters into vortex ring state, turbulent wake state and windmill brake state and momentum theory does not hold for these states. Hence, stability analysis with simple momentum theory cannot be conducted on axial wind from the bottom of the rotor.

Chapter 4: Height and Speed Estimation

4.1 Grid-based Recursive Bayesian Filter

The Bayesian filter [13] [23] is a probabilistic approach for estimation that assimilates noisy measurements into a probability density function (PDF) using nonlinear system dynamics and observation operators. The optimal Bayesian filter for linear systems with linear measurements and Gaussian noise is the Kalman filter [24], whereas a common Bayesian filter for nonlinear systems with nonlinear observation and noise models is the particle filter [25].

A grid-based recursive Bayesian filter can be rapidly implemented for a low-dimensional state-space representation of the rotorcraft downwash with linear parameter estimates and a nonlinear measurement model. It is of note that even though linear paramater estimates and Gaussian white noise is assumed for my measurement and process noise, these are not required assumptions for the Bayesian filter.

Familiar estimation tools in the literature, such as the Kalman filter and the Extended Kalman filter, were not used as they require linear observation models. Other tools such as the Unscented Kalman filter (UKF) [26], Ensemble Kalman Filter [27] and Particle filter [25] allow for nonlinear dynamics and measurement

models. As an alternative, the Unscented Kalman filter [26] is an approximate nonlinear estimator that differs the inevitable divergence with highly nonlinear systems or measurements and approximates the estimated PDF as a Gaussian distribution. [24]. The Ensemble Kalman filter typically requires a sampling ensemble size of 50 to 100 for the estimation of thousands of states [27], with applications such as weather forecasting. The particle filter provides high performance estimation but it requires careful selection of its estimation state vector because it is prone to sample impoverishment, requires careful tuning and comes at a higher computational cost. Simon [24] derives and compares these other filters while detailing their applications and limitations.

Fig. 4.1 shows the general principles of a grid-based recursive Bayesian filter. I begin with prior knowledge of the estimated system state that is expressed in terms of a PDF. The next step involves collecting measurements and evaluating the likelihood that the measurement resulted from a nearby state. The likelihood function is then assimilated with the prior PDF according to Bayes's theorem to generate a posterior PDF. A prediction is made by shifting and diffusing the posterior using the system dynamics and process noise. The estimation is finally made by taking the mode of the final PDF and the process is repeated.

4.2 Estimation Step

The Bayesian framework consists of the estimation and the prediction step. In the estimation step, the Bayesian filter in the form of [13] estimates the vehicle

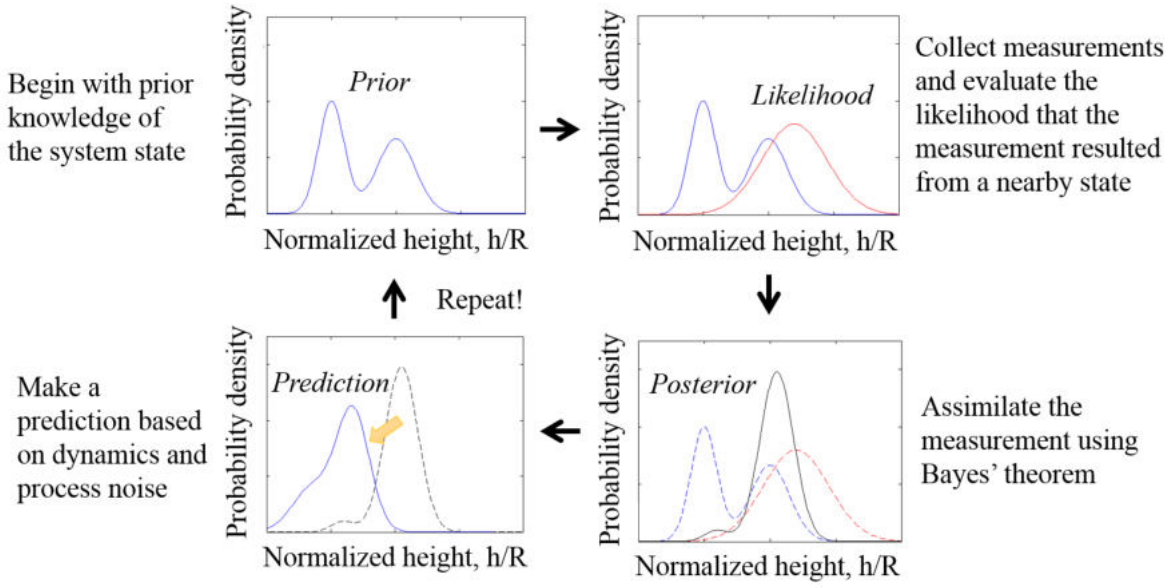

Figure 4.1: General principles of grid-based recursive Bayesian filter. Credit: Frank D. Lagor.

height based on the flow-velocity measurements from an array of differential pressure sensors. Grid-based Bayesian estimation is performed recursively, in which the finite parameter space over height h is discretized and the PDFs are evaluated on this grid for each new measurement. Let h be the single state of a one-dimensional Bayesian filter. Recall that the noisy flow measurement $\tilde{V}$ is corrupted with zero mean Gaussian noise as in (2.12). Let $L = \{\tilde{V}_1, ..., \tilde{V}_m\}$ denote the set of observations from m sensors. Note that each velocity component measurement (even at the same location) is treated as a separate measurement. The posterior probability of the state h given the measurements L is [13]

$$P(h|L) = cP(L|h)P(h|L_0), \tag{4.1}$$

where c is the scaling factor chosen so that $P(h|L)$ has unit integral over the state space. The likelihood function $P(L|h)$ is the conditional probability of the observations L given the state h and $P(h|L_0)$ represents the prior probability distribution. During initialization or in the absence of measurements, the prior probability $P(h|L_0)$ is uniform.

I choose a Gaussian likelihood function for the measurements $\tilde{V}_l, l = 1, ..., m$, i.e.,

$$P(\tilde{V}_l|h) = \frac{1}{\sqrt{2\pi}\sigma}\exp\left[-\frac{1}{2\sigma^2}(\tilde{V}_l - V_l)^2\right], \tag{4.2}$$

where V_l is the flow at height h generated from the flow model (2.10) or (2.11) and σ^2 is the measurement variance. The posterior probability density of the state h is obtained using the joint measurement likelihood combining the measurements taken from all m sensors [13], i.e.,

$$P(h|L) = c\left(\prod_{l=1}^{m} P(\tilde{V}_l|h)\right)P(h|L_0). \tag{4.3}$$

The estimated height $\hat{h}$ corresponding to the mode (supremum) of the posterior probability $P(h|L)$ provides the maximum likelihood estimate of the flowfield parameters.

Spatial integration over the sensor array is accomplished by (4.3), whereas temporal integration is accomplished by assigning the posterior of the current time step to be the prior for the next time step.

4.3 Prediction Step

The prediction step consists of shifting and diffusing the probability mass to account for the vehicle dynamics using the Chapman-Kolmogorov equation [25],

$$\begin{aligned} &P(h(t+\Delta t)|L(t)) \\ &= \int P(h(t+\Delta t)|h(t))P(h(t)|L(t))dh(t), \end{aligned} \tag{4.4}$$

where t is the current time step and Δt is the time step interval. Numerically, the probability density is shifted along the grid according to the estimated speed $\hat{z}_2$. If the estimated speed $\hat{z}_2$ is positive, I shift the PDF to the right and vice-versa. The number of grid points to shift is determined by the product of the estimated speed $\hat{z}_2$ and time interval. After shifting, the probability density is normalized to ensure the PDF integrates to one.

To account for uncertainty in the motion model, the probability density is diffused with process noise κ by convolution with a grid-sized Gaussian window whose width is inversely proportional to the standard deviation of the process noise σ_κ. (This step is done with the MATLAB functions `gausswin` and `convn`.)

4.4 Prefiltering and Filter Tuning

4.4.1 Prefiltering

It was observed that the measurements collected were extremely noisy, which causes unreliable estimation even after significant Bayesian filter tuning efforts. In order to improve the performance of the filter, an extra prefiltering step was introduced to prefilter the noisy measurements before they are passed into the Bayesian filter. Given the corrupted measurement $\tilde{V}$ from (2.12), the goal is to compute an estimate $\hat{V}$ of the original velocity component signal V through a process known as signal reconstruction, which is also known as denoising or smoothing [28].

The quadratic smoothing convex optimization method is implemented. The reconstruction method uses the quadratic smoothing function [28]

$$\Lambda_{quad}(V) = \sum_{i=1}^{n-1}(V_{i+1} - V_i)^2 = \|DV\|_2^2, \tag{4.5}$$

where V is the velocity component signal I wish to reconstruct and $D \in \mathbb{R}^{(n-1)xn}$ is the bidiagonal matrix

$$D = \begin{bmatrix} -1 & 1 & 0 & ... & 0 & 0 & 0 \\ 0 & -1 & 1 & ... & 0 & 0 & 0 \\ ... & ... & ... & & ... & ... & ... \\ 0 & 0 & 0 & ... & -1 & 1 & 0 \\ 0 & 0 & 0 & ... & 0 & -1 & 1 \end{bmatrix}. \tag{4.6}$$

The optimal trade-off between $\|\hat{V} - \tilde{V}\|_2$ and $\|D\hat{V}\|_2$ is obtained by minimizing [28]

$$\|\hat{V} - \tilde{V}\|_2^2 + \delta\|D\hat{V}\|_2^2, \tag{4.7}$$

where $\delta > 0$ parametrizes the optimal trade-off curve. The solution to this quadratic problem is [28]

$$\hat{V} = (I + \delta D^T D)^{-1}\tilde{V}, \tag{4.8}$$

and it can be efficiently computed as $I + \delta D^T D$ is tridiagonal [28].

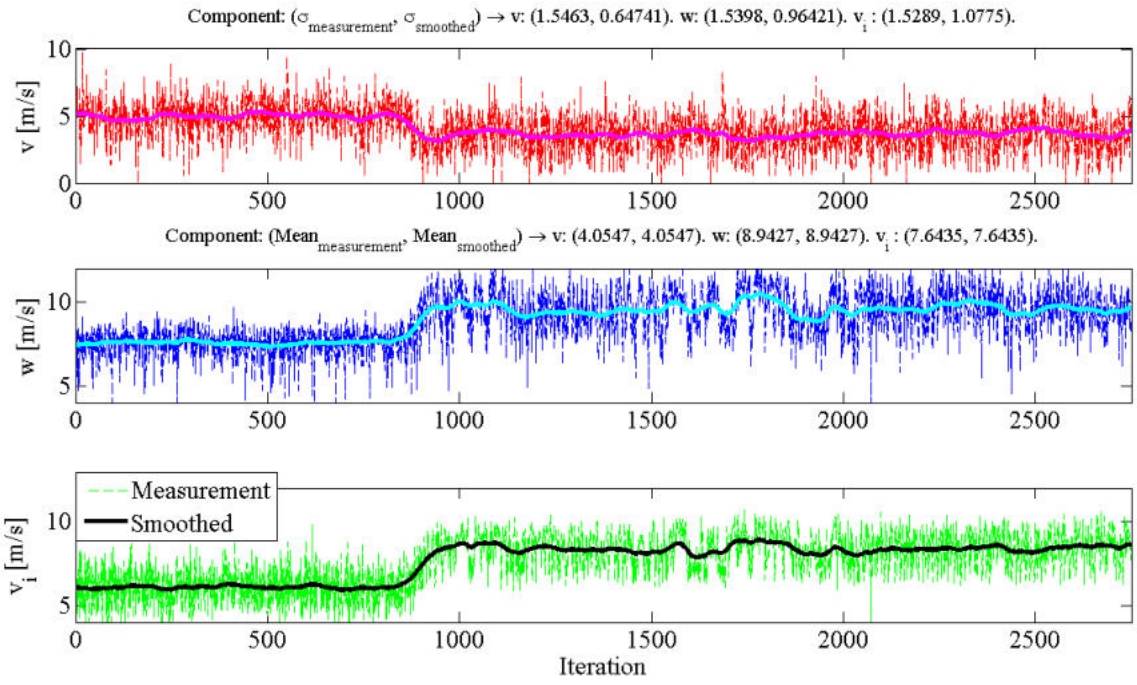

Figure 4.2: Comparison between measurements and quadratically smoothed values of velocity components.

Fig. 4.2 shows the comparison between measurements $\tilde{V}$ and quadratically smoothed values of the velocity components $\hat{V}$, with $\delta = 500$. The trends of the

measurements are still preserved in the smoothed values and the mean of both values are identical. Most importantly, the standard deviations of the smoothed values for u, v, w are reduced compared to that of the measurements, which means that the Bayesian filter can trust the smoothed values more and focus on estimation.

4.4.2 Filter Tuning

The standard deviations of measurement noise σ_η and process noise σ_κ in the Bayesian filter can be used as tuning knobs to improve the filter performance in terms of estimation accuracy and convergence speed. Simple statistical analysis such as computing the mean and standard deviation of the measurements in hover is useful for figuring out the nominal values.

The value of σ_η for each measurement signifies how much the Bayesian filter should trust the measurement, with a higher value implying noisier measurements. The ratios between σ_η for u, v and w is an indicator of how noisy each measurement is relative to each other. Standard deviation of the process noise σ_κ is an indicator of the system dynamics speed. Higher values of σ_κ signify that the state space evolves quickly. By tuning σ_η and σ_κ, the accuracy of the estimates can be improved.

Another pertinent issue is the convergence speed of the filter, which is an indicator of the time required for convergence between the actual height and estimated height. Ideally, I want a fast observer that converges to the actual height as quickly as possible. The convergence speed is also determined by σ_η and σ_κ. $\sigma_\eta >> 1$ implies a slow observer because the filter trusts the measurements less and has to

extract the trends of the noisy measurements. On the other hand, $\sigma_\kappa >> 1$ implies a fast observer because larger process noise indicates faster dynamics which allows the observer to converge to different heights quickly.

4.5 Speed Estimation

The vertical velocity $\hat{z}_2$ is estimated from the estimated height $\hat{z}_1$ by finite differencing, i.e.,

$$\hat{z}_{2,p} = \alpha \hat{z}_{2,p-1} + (1-\alpha)\frac{\hat{z}_{1,p} - \hat{z}_{1,p-1}}{\Delta t}, \tag{4.9}$$

where $0 < \alpha < 1$, the index p indicates the current time step and Δt is the time interval between each simulation step. Eq. (4.9) is a low-pass-filter that removes most of the effects of noise.

Chapter 5: Control Design

The controller is designed and implemented for height tracking operations which include hover, climb and descent to new equilibrium heights and landing. Design requirements for these operations include short rise time, small overshoot and steady-state error. Three controllers are designed, which include an optimal Linear Quadratic Regulator (LQR) and a Proportional-Integral (PI) controller with Feedforward. The LQR controller is verified in simulation, while the PI-Feedforward controller is implemented on the heave test stand.

5.1 Linear Quadratic Regulator

Given the linear system dynamics (3.25) with known states Z, non-zero initial conditions $Z(0)$ and noiseless dynamics, the optimal control ν which takes the system to zero state ($Z = 0$) is the Linear Quadratic Regulator (LQR) problem. The optimal control ν is computed by minimizing the cost function [29]

$$J = \int_0^\infty (Z^T Q Z + \nu^T S \nu) dt, \tag{5.1}$$

where Q and S are appropriately chosen constant weighting matrices such that $Q = Q^T \geq 0$ and $S = S^T \geq 0$. The optimal solution for any initial state which minimizes the cost function is the full-state feedback control input $\nu = -KX$ [29] where

$$K = S^{-1}B^T X, \tag{5.2}$$

and $X = X^T \geq 0$ is the unique positive-semidefinite solution of the algebraic Riccati equation [29]

$$E^T X + XE - XFS^{-1}F^T X + Q = 0. \tag{5.3}$$

5.1.1 LQ Full State Feedback Control

The state space system of a rotorcraft IGE (3.25) in control affine form is

$$\dot{Z} = f(Z) + g(Z)\nu_2, \tag{5.4}$$

where

$$f(Z) = \begin{bmatrix} z_2 \\ \\ -g \end{bmatrix} \quad \text{and} \quad g(Z) = \begin{bmatrix} 0 \\ \\ \frac{16z_1^2}{16z_1^2 - R^2} \end{bmatrix}. \tag{5.5}$$

Fig. 3.4 shows that the constant-input open-loop nonlinear system with $\nu_2 = \nu_2^*$ oscillates about the equilibrium point, which implies that feedback control is needed

to asymptotically stabilize z_1 to the desired height. A linear controller to be used with the nonlinear system dynamics is

$$\nu_2 = \nu_2^* + \Delta\nu_2, \tag{5.6}$$

where $\Delta\nu_2 = -K(Z - Z^*)$ and $K = [K_1 \quad K_2]$. The closed-loop dynamics with the linear full state feedback controller (5.6) are

$$\dot{Z} = \begin{bmatrix} z_2 \\ -g \end{bmatrix} + \begin{bmatrix} 0 \\ \frac{16z_1^2}{16z_1^2 - R^2} \end{bmatrix} (\nu_2^* + \Delta\nu_2), \tag{5.7}$$

i.e.,

$$\dot{Z} = \begin{bmatrix} z_2 \\ -g + \frac{16z_1^2}{16z_1^2 - R^2} \left(g\frac{16z_1^{*2} - R^2}{16z_1^{*2}} - K_1(z_1 - z_1^*) - K_2 z_2 \right) \end{bmatrix}. \tag{5.8}$$

The gains K_1 and K_2 are chosen by LQR (5.2).

If the states of the system are assumed to be known, LQ full-state feedback control can be implemented using the linear controller (5.8). Figure 5.1 compares the nonlinear closed-loop dynamics (5.8) to the linear closed-loop dynamics (3.13), using linear controller (5.6). The Jacobian matrices in (3.26) are evaluated at the equlibrium height. Initial conditions for the height and speed are (1.8m, 0.9m/s) and desired steady-state conditions are (0.75m, 0m/s).

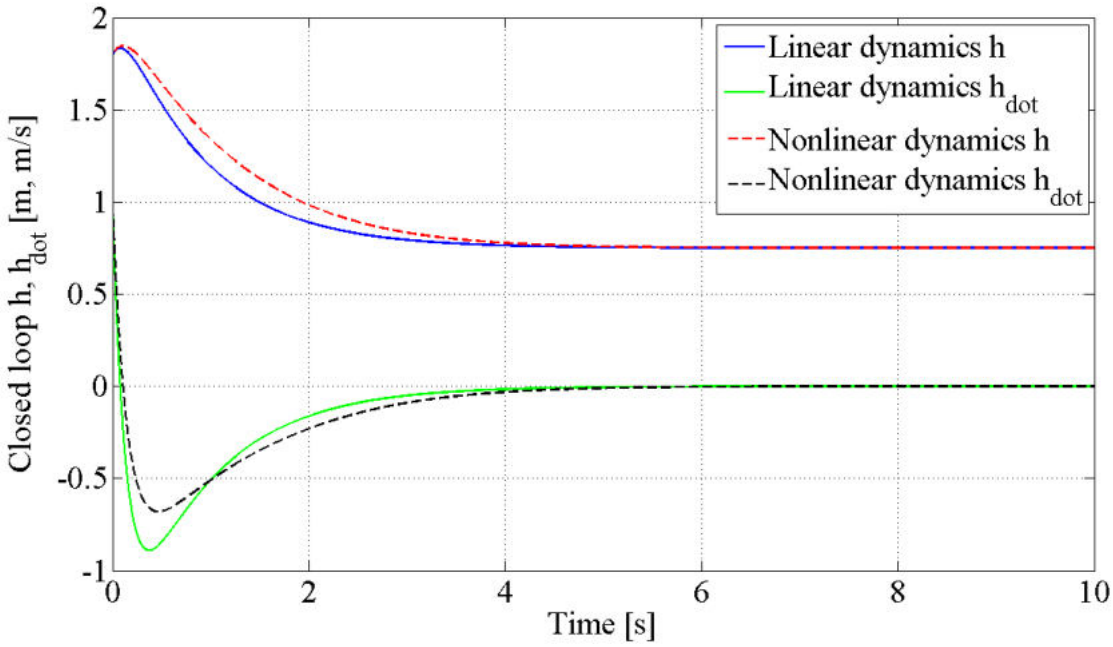

Figure 5.1: Closed-loop dynamics of rotorcraft in ground effect with full-state feedback using the linear controller (5.6).

5.1.2 LQ Observer-based Feedback Control

Lack of knowledge of actual states of the system is common in most real-world applications. As such, observers or filters are typically implemented to estimate these states and the observed states are then used for feedback control. I can estimate the height z_1 of my rotorcraft IGE using a Bayesian filter and the vertical speed z_2 using (4.9). With these estimates, I can implement an LQ observer-based feedback control with (5.8) by letting $Z = \hat{Z}$.

Fig. 5.2 shows the evolution of the posterior probability density of estimated height during Bayesian filter-based closed-loop ascent (Fig. 5.2(a)) and descent (Fig. 5.2(b)). Fig. 5.2(a) shows an ascent maneuver from initial normalized height and speed (with respect to R) of (0.7, 0/s) to a commanded height of 1.8 and process and

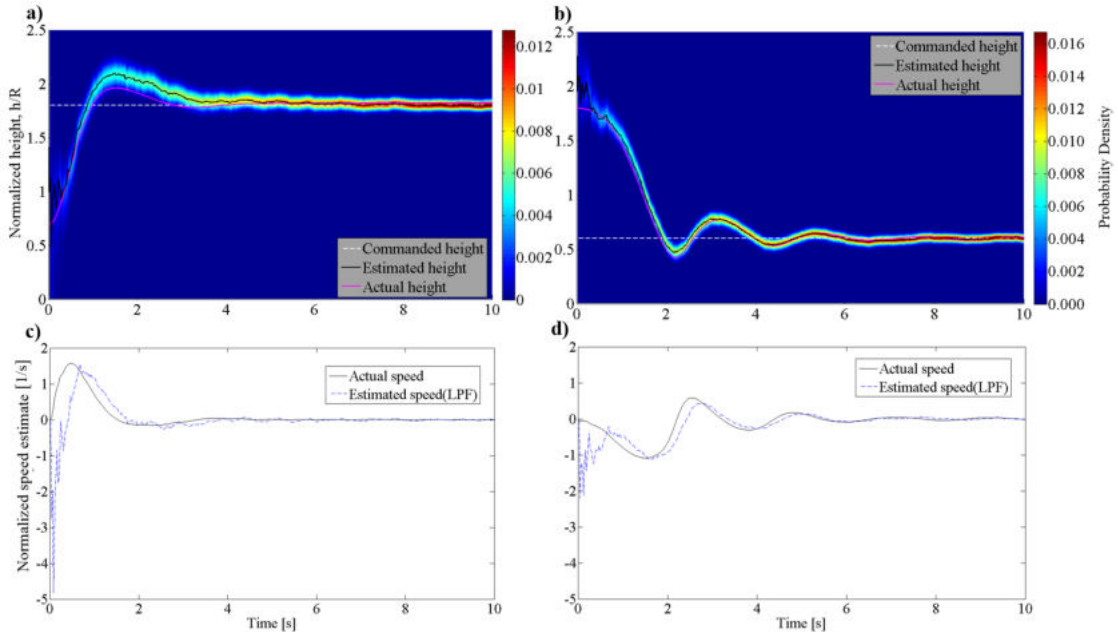

Figure 5.2: Simulations of the closed-loop control system with estimated height using the Bayesian filter framework show the posterior probability density of normalized height h/R and normalized speed plotted versus time. (a) Ascent maneuver from initial height and speed of (0.7, 0/s), commanded height of 1.8 and process and measurement noise standard deviation of (0.1, 0.15/s); (b) descent maneuver from initial height and speed of (1.8, 0.2/s), commanded height of 0.6 and process measurement noise standard deviation of (0.08,0.1/s); (c) estimated speed using low-pass-filtered (LPF) finite differencing for ascent maneuver in (a); (d) estimated speed using low-pass-filtered (LPF) finite differencing for descent maneuver in (b).

measurement noise standard deviation of (0.1, 0.15/s). Fig. 5.2(b) shows a descent maneuver from initial height and speed of (1.8, 0.2/s) to a commanded height of 0.6 and process and measurement noise standard deviation of (0.08, 0.1/s). Fig 5.2(c) and (d) show the estimated speeds using the low-pass-filtered finite-differencing method (4.9) for ascent in (a) and descent in (b), respectively.

These manuevers are simulated using the closed-loop dynamics (5.8) with $Z = \hat{Z}$. Process noise κ, which is Gaussian white noise with standard deviation σ_κ and zero mean, is added to (5.8) in the filter. The estimated height $\hat{z}_1$ is evalu-

ated recursively by the one-dimensional Bayesian filter. The vertical velocity $\hat{z}_2$ is estimated using the finite-difference low-pass filter method (4.9).

Fig. 5.2(a) and (b) show that the initial height estimation error is large because the prior PDF is uniformly distributed. As the Bayesian filter assimilates measurements over time, the posterior probability density peaks and the estimated height converges to the actual height. As more measurements are taken, the filter narrows the probability density. Note that Fig. 5.2(a) has a bigger spread throughout its probability density distribution than Fig. 5.2(b), due to the higher noise variances.

Fig. 5.2(c) and (d) show that the initial speed estimates are relatively large as the difference between succesive height estimations is also relatively large. This effect is influenced by the Bayesian filter initiation and also the controller, which is driving the system to the comanded height. As the system reaches steady state at about 4s, the speed estimates begin to more closely track the actual speed. The first-order speed estimation could be improved by using a higher-order estimation method.

5.2 Proportional Integral (PI) Controller with Feedforward

As shown in Fig.5.3, a Proportional Integral (PI) controller with feedforward is implemented on the heave test stand due to its ease of implementation. The heave test stand is actuated with a brushless motor that is controlled with an Electronic Speed Controller (ESC) that takes Pulse Width Modulation signals as control in-

put for motor rotational speed regulation. The PWM control input from feedback control is computed with a PI controller

$$\nu_{PI} = K_P(z_1^* - \hat{z}_1) + K_I \int (z_1^* - \hat{z}_1)dt, \tag{5.9}$$

where K_P and K_I are the proportional and integral gains.

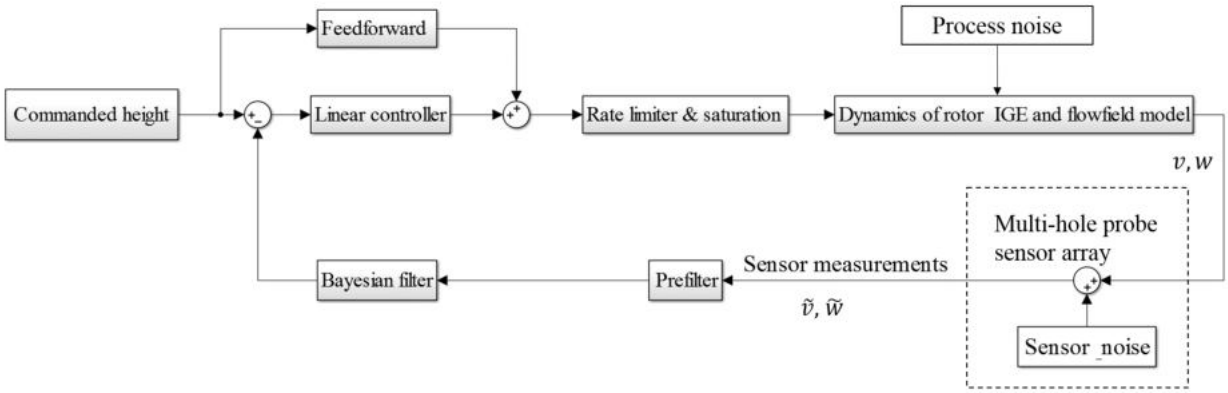

Figure 5.3: Block diagram of Proportional Integral controller with feedforward.

Feedforward control is typically used to speed up the closed-loop system response and compensate for unmodeled dynamics by feeding in set inputs. I implemented the feedforward controller in order to compensate for the transient dynamics of the brushless motor-ESC, which is dissimilar from the steady-state dynamics. The feedforward control input $\nu_{FW}$was based on a curve fit for the open-loop transient PWM-height curve shown in Fig. 5.4. The sum of the feedback and feedforward control inputs

$$\nu_1 = \nu_{PI} + \nu_{FW} \tag{5.10}$$

are then rate limited and saturated before being input into the ESC.

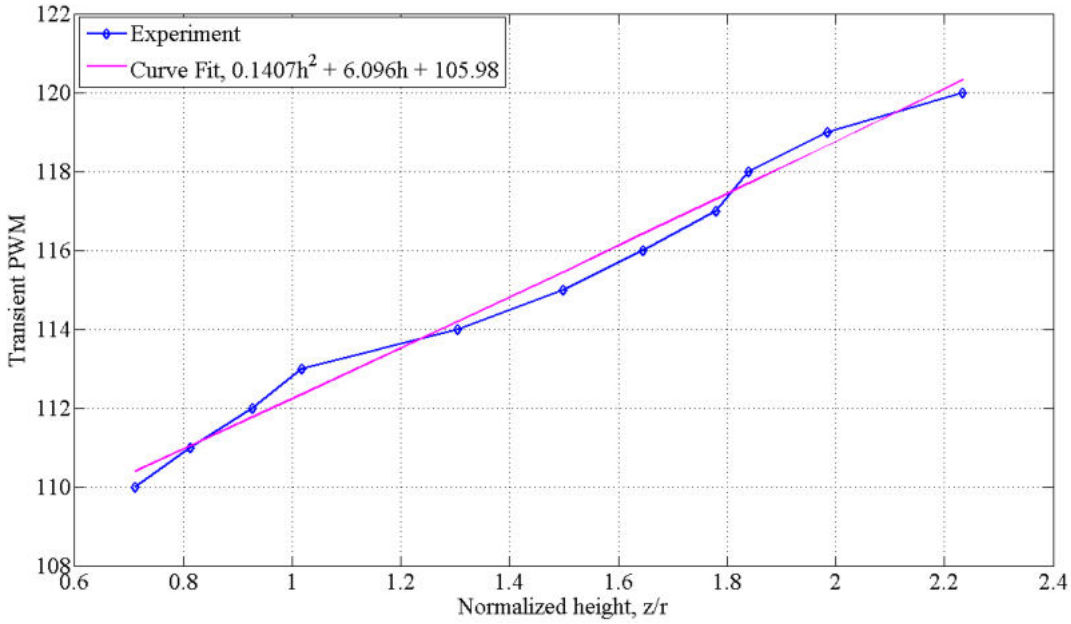

Figure 5.4: Open-loop transient PWM versus height for feedforward controller.

Chapter 6: Experimental Setup and Validation of Flow Model

6.1 Test Setup

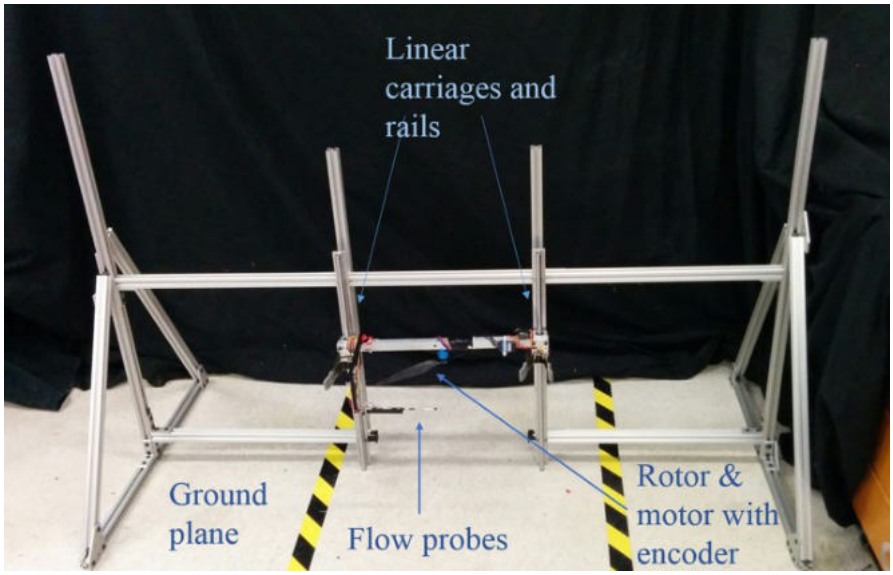

Figure 6.1: Static-height test stand.

Experiments were conducted to verify and implement the theoretical framework presented in the previous chapters. These experiments were conducted on two experimental test stands. The dynamic compound pendulum heave test stand is shown in Fig. 3.1, while the static-height test stand is shown in Fig. 6.1.

The static-height test stand was built with linear carriages and rails in a vertical configuration and it was observed that this configuration was not sufficiently smooth. As such, the static-height test stand was used to collect measurements of

radial v and vertical w velocity components at static heights.

6.2 Experimental Instrumentation

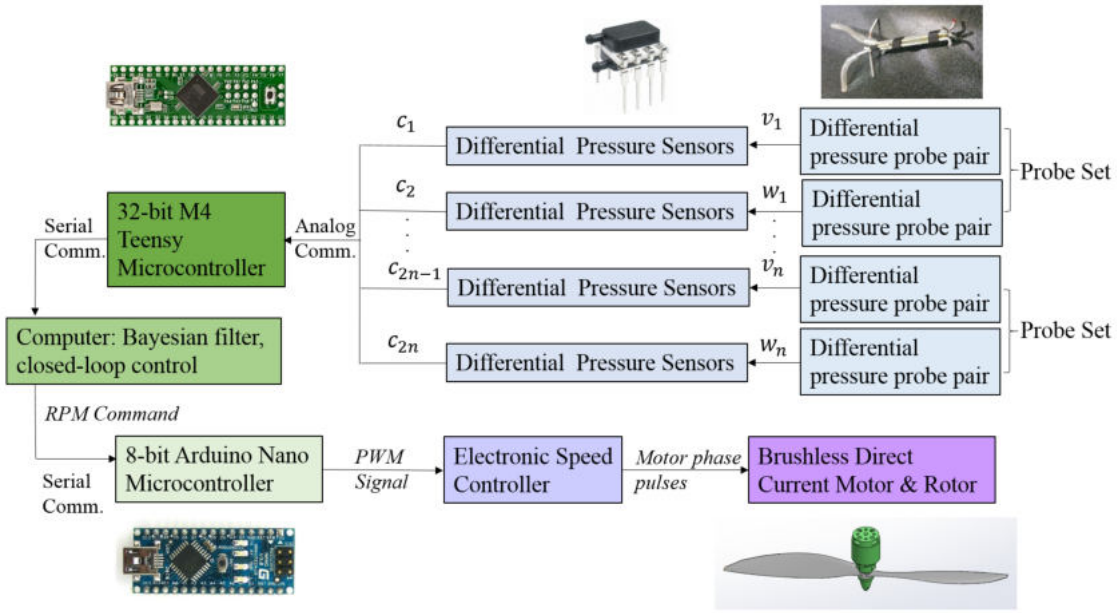

Figure 6.2: Block diagram for experimental instrumentation.

Fig. 6.2 shows a block diagram of the experimental instrumentation, which is categorized into three parts: sensing (blue), estimation and control (green) and actuation (purple). The differential pressure probe sets are connected to differential pressure sensors to measure radial and vertical flow pressure. The pressure measurements are then collected by a Teensy microcontroller for prefiltering and conversion into velocity components. These velocity measurements are transmitted to the computer for height estmation and closed-loop control. The actuation of the experimental setup consists of a Brushless Direct Circuit (BLDC) motor and Electronic Speed Controller (ESC) pair. Speed-control input requires Pulse Width

Modulation (PWM) square wave signals with variable timescales, which are generated by the RC receiver or Arduino Nano microcontroller according to control inputs from the computer. All physical data connections are made through Universal Serial Bus (USB) cables.

Table 6.1: Experimental Equipment.

Equipment	Model & Make
Brushless Direct Circuit Motor	850Kv AC2830-358
Differential Pressure Sensors	Honeywell HSCDRRN001NDAA3
Direct Circuit Power Supply	Mastech HY3030E
Electronic Speed Controller	eRC Rapid Drive 25A
Modular Aluminum Profiles	MakerBeam & 8020
Microcontroller: Data Acquisition	Cortex-M4 Teensy 3.1
Microcontroller: Motor Speed	ATmega328 Arduino Nano
Remote Control Radio	Spektrum DX6i
Rotor	HobbyKing 14X4.7 Carbon Fiber
Motion Capture Facility	OptiTrack Flex 3

Table 6.1 lists the make and model of the experimental equipment. Note that the Remote Control (RC) radio is used for manual motor-speed control, whereas the Arduino Nano microcontroller is used for automatic speed control. My scaled rigid rotor has rotor radius $R = 17.78$ cm (7 in.).

A differential pressure probe set that is capable of measuring the radial and vertical differential pressure consists of two pairs of tubes, as shown in Fig. 6.3. Each pair is connected to a differential pressure sensor [11]. The pressure sensors are connected via an analog interface to the Teensy 3.1 Microcontroller for Data

Figure 6.3: Two-pair differential pressure probe set providing radial and vertical velocity components after conversion.

Acquisition (DAQ). Since the pressure measurements are relatively noisy and the pressure sensor and DAQ microcontroller are capable of higher data rates than the estimation and control loop in the computer, a Moving Average Filter (MAF) is implemented on the pressure measurements to generate velocity measurements $\tilde{V}$. The MAF implementation is

$$\tilde{V} = \frac{p}{J} \sum_{j=1}^{J} \tilde{P}_j, \tag{6.1}$$

where $\tilde{P}_j$ is the instantaneous measurement from the differential pressure sensor, J is the number of datapoints to average over and p is the conversion factor from differential pressure to velocity [11].

Fig. 6.4 shows the instrumentation setup for the compound pendulum heave test stand, which is similar to that of the static heave test stand. Motion capture (MoCap) markers are mounted on the probe bracket for height ground truth. Two different probe configurations are mounted on the probe bracket, which are the single pair and two pair sets. The single probe pair is placed close to the rotor

plane to measure the vertical differential pressure which corresponds to the induced velocity. This measurement is used as an input to the ring-source potential flow models (2.10) and (2.10). The two pair probe set is capable of measuring both radial and vertical differential pressures. In order to reduce inter-probe interference, the induced velocity probe is mounted azimuthally 180° away from the two pair probe set and all probes are mounted above the probe bracket directly into the rotor flowfield.

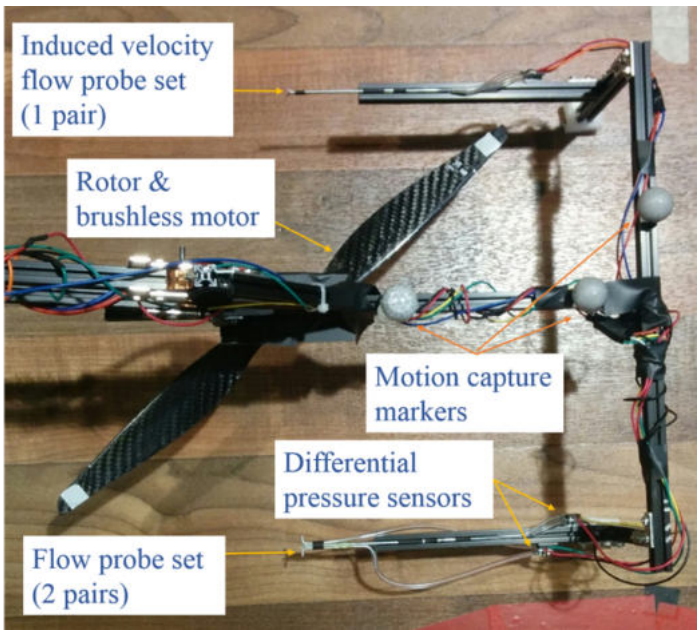

Figure 6.4: Compound pendulum heave test stand instrumentation.

6.3 Flow Model Validation for Varying Radial Locations

Fig. 6.5 compares the measured radial and vertical velocity components with the flow model at multiple radial stations for normalized height $h/R = 0.75$. The data is filtered with $J = 10^5$ data points in the MAF (6.1). The average of five consecutive measurements are plotted. Error bars on the measured values show the

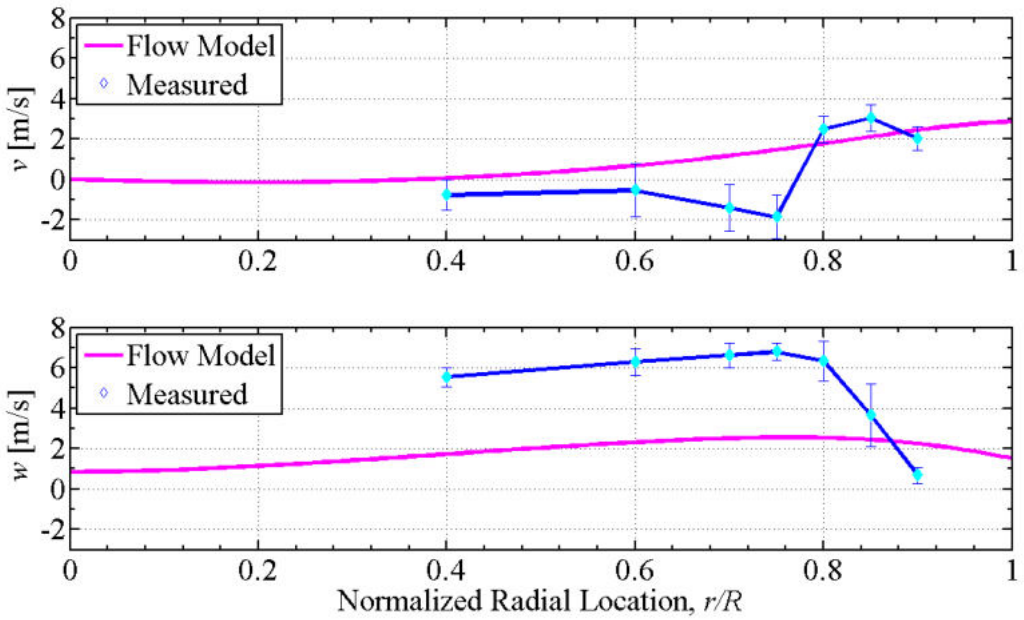

Figure 6.5: Comparison between ring-source potential flow models (2.10), (2.11) and experimental results of radial v and vertical w velocity components for various radial locations. Error bars on the measured values indicate one standard deviation away from the mean. Normalized height $h/R = 0.75$, normalized probe location z/R= 0.18, rotational speed ω=2538 RPM, induced velocity IGE $v_i = 4.34$m/s.

values one standard deviation away from the mean. The probes are placed at vertical location $z/R = 0.18$ from the rotor plane, the motor rotational speed $\omega = 2538$ RPM and induced velocity IGE $v_i = 4.34$ m/s. The induced velocity IGE is the average of vertical velocities close to the rotor plane across multiple radial locations and, in this case, the induced velocity probes are at vertical location $z/R = 0.05$.

The measured radial velocity v crosses over from positive to negative at r/R=0.75, which represents suction toward the rotor hub. Taking the standard deviations into account, some of the radial measurements agree with the model, but the model does not predict the velocity sign changes. This is due to the geometry of the ring sources because inward flow at opposite sides of the same ring cancel out and radial velocity is always outward and positive. Furthermore, the radial flow is also influenced by

turbulence and the tip vortices of each rotor blade, whereas the flow model only captures the mean velocity.

The measured vertical velocity w increases with increasing radial station from z/R= 0.4–0.75 and then decreases rapidly for the outboard section. The model predicts a similar trend of increasing vertical velocity with increasing radial station and gradually tapering off at approximately the same radial station as the measurement but still underpredicts the vertical velocity component. The underprediction is likely because the induced velocity used in this flow model is an average rather than the local value. Another effect that my flow model does not model is the tip losses due to tip vortices. Despite being a highly reduced-order potential flow model which doesn't model the unsteady aerodynamics and tip vortices, the model still captures the general trend of both radial and vertical velocities.

6.4 Probe Placement and Flow Model Validation for Varying Heights

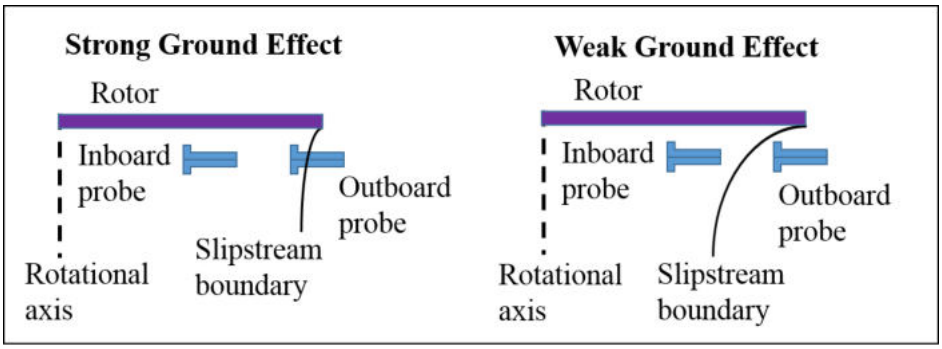

Figure 6.6: Probe placement in strong and weak ground effect.

Probe placement is affected by many factors, but most importantly, the probes have to be well within the rotor slipstream boundary in order for the model to

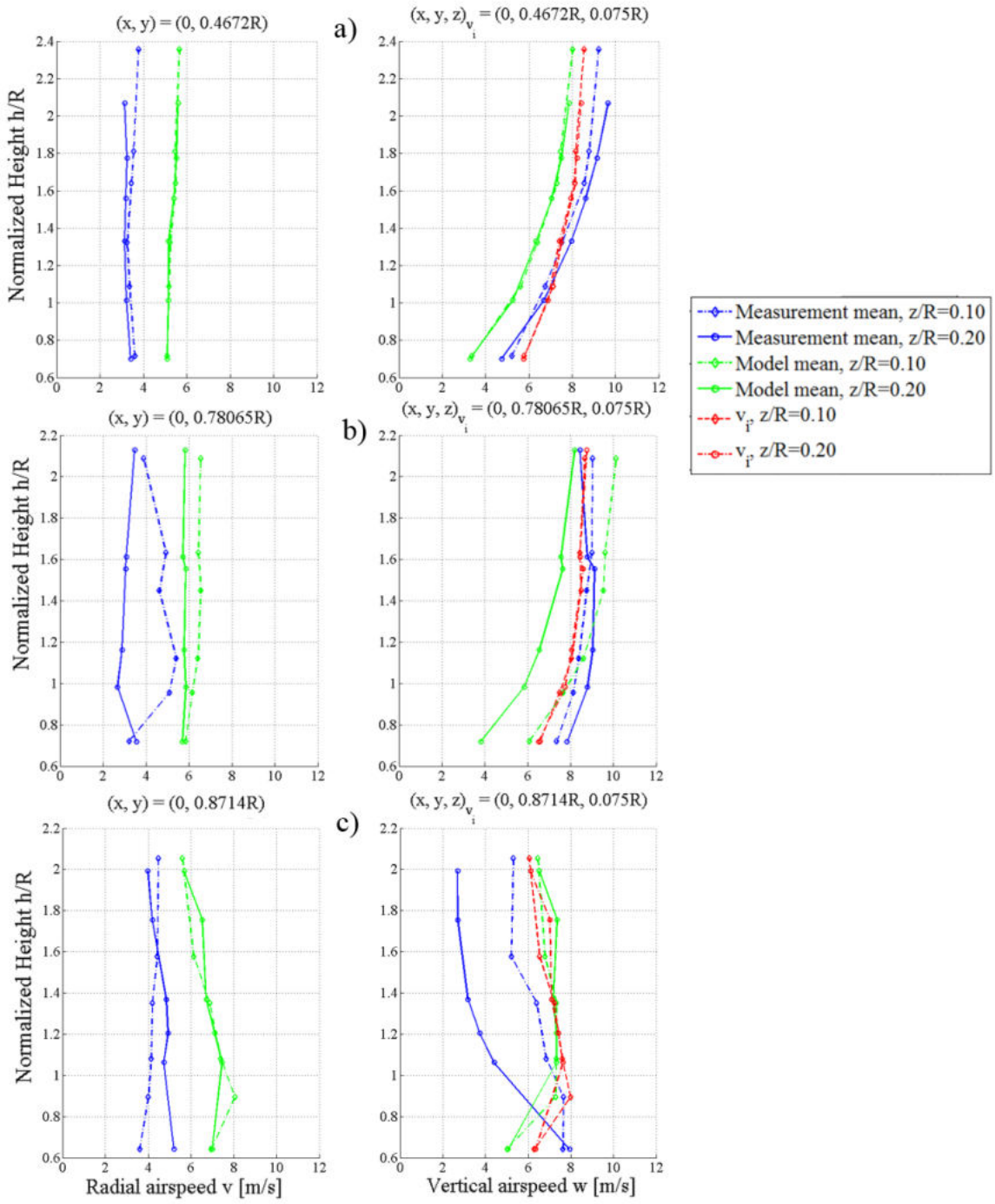

Figure 6.7: Comparison between ring-source potential flow models (green) and experimental results (blue) of radial v, vertical w and induced v_i (red) velocity components for varying heights. Experiments were conducted on the compound pendulum heave test stand with probe vertical locations of $z/R = 0.1$ (solid circle) ,0.2 (dashed diamond) and $z_{v_i} = 0.075$. The probes are radially symmetrical at (a) $(x, y) = (0, 0.4672R)$; (b) $(x, y) = (0, 0.7807R)$; (c) $(x, y) = (0, 0.8714R)$.

match the measurements, as shown in Fig. 6.6. Note that the figure is merely an illustration and for any given experiment, either the inboard or outboard probe is mounted and not both together in order to minimize inter-probe interference. The following experiments illustrate the importance of proper probe location.

Fig. 6.7 compares the ring-source potential flow models (green) (2.10), (2.11) with experimental results (blue) of radial v, vertical w and induced v_i (red) velocity components for varying heights. Experiments were conducted on the compound pendulum heave test stand with probe vertical locations of $z/R = 0.1$ (solid circle) , 0.2 (dashed diamond), $z_{v_i} = 0.075$ and radially symmetrical probe locations at (a) $(x, y) = (0, 0.4672R)$; (b) $(x, y) = (0, 0.7807R)$ and (c) $(x, y) = (0, 0.8714R)$. The induced velocity probe measures local induced velocity which is used as an input into the potential flow model.

For probe locations at $(x, y) = (0, 0.4672R)$, Fig. 6.7(a) shows relatively constant radial velocity v measurements for increasing height. The vertical velocity w measurements increase for increasing height and decreasing vertical probe location. The flow model captures the general trends even though it overpredicts the radial velocity v and undepredicts the vertical velocity w. These prediction trends are similar to those shown in Fig. 6.5, but the difference between measured and predicted vertical velocity w is smaller for this experiment. This is likely caused by the local induced velocity v_i at a radially symmetrical location being input into the flow model as opposed to the average for the previous experiment.

For probe locations at $(x, y) = (0, 0.7807R)$, Fig. 6.7(b) shows that the radial velocity measurements v begin to fluctuate for decreasing vertical probe location

while the model stays relatively flat. The vertical velocity w measurements also display similar trends to that of (a) but they begin to decrease after $h/r = 1.5$, which is not captured by the model. The decrease in w and fluctuations in v are likely caused by the probes being closer to the edge of the slipstream boundary and the effects of tip vortices becoming more profound. The slipstream boundary contracts more as the setup moves to greater heights and the ground effect becomes weaker, which causes the vertical velocity w to be slower as the probes are closer to the tip and the radial velocity v to fluctuate. Since the model does not model tip vortices, these detailed effects are not captured. The general trends are somewhat captured at this radial station for (b), albeit not as well as for the inboard case in (a).

Finally, for probe locations at $(x, y) = (0, 0.8714R)$, Fig. 6.7(c) shows that the radial velocity v measurements decrease with increasing height for $z/R = 0.20$ and then increase slightly with decreasing height for $z/R = 0.10$. The general trend is similar for the model, which still overpredicts the measurements. The vertical velocity w measurements for both vertical sensor locations decrease with increasing heights. However, the model diverges from the measurement trends and its vertical velocity w still increases for increasing height and then tapers off. The divergence is caused by the (outboard) probe being clearly outside the slipstream boundary, as shown in Fig. 6.6. Once the probe is outside the slipstream boundary, it is no longer measuring the flowfield due to ground effect but rather the flowfield outside the rotor wake, which is not modeled by the ring-source potential flow model.

Since tip effects are not captured within the flow model, probe placement has a

signifcant effect on measurement-model mismatch. In fact, a nominal 12% increase in the radial location from $y = 0.7807R$ to $0.8714R$ places the probe well outside the slipstream boundary and causes model divergence. Hence, as shown in Fig. 6.8, it is highly recommended that the probes be placed in a radially symmetrical fashion at about mid-radius where tip effects aren't as significant and the model captures the general trends of the measurements within the operational region of ground effect.

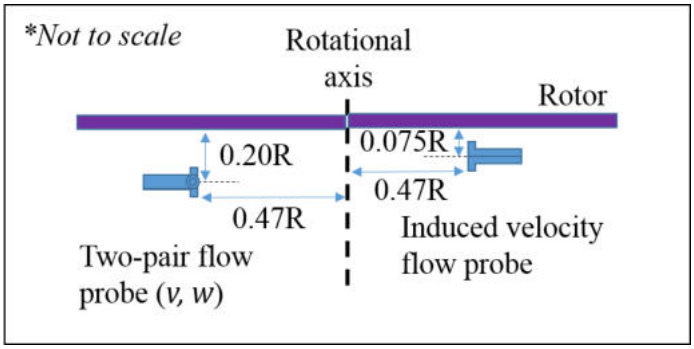

Figure 6.8: Rotor side view showing recommended mid-radius location with radial symmetricity for both two-pair flow probes (radial v and vertical w velocity components) and induced velocity v_i flow probe.

Chapter 7: Validation of Estimation and Observer-based Feedback Control

7.1 Validation of Height Estimation Framework

An experiment was conducted for the purpose of validating the height estimation framework. The experiment was flow-sensing based Bayesian height estimation and closed-loop control using the actual height provided by the motion capture facility. The grid-based recursive Bayesian height estimation was implemented with (4.3) and the closed-loop control was performed with a PI and feedforward controller (5.10). The probes are radially symmetrical at $(x, y) = (0, 0.4672R)$, $z/R = 0.20$ and $z_{v_i}/R = 0.075$. The standard deviation for measurement (v, w) and process noise are (4.8, 2.4, 10). The measurements are prefiltered by means of $J = 50$ points in the MAF (6.1) and $\delta = 500.$ for quadratic smoothing (4.8).

Fig. 7.1 shows the experimental results which validates the height estimation framework. Fig. 7.1(a) shows the commanded heights in black. The heave stand was initiated at normalized height $z/r = 0.75$ and ascended to $z/r = 1.6$ and then descended to $z/R = 1$. The height estimates (blue) are plotted against ground truth (red) provided by MoCap. The filter response was satisfactorily fast and tracked the

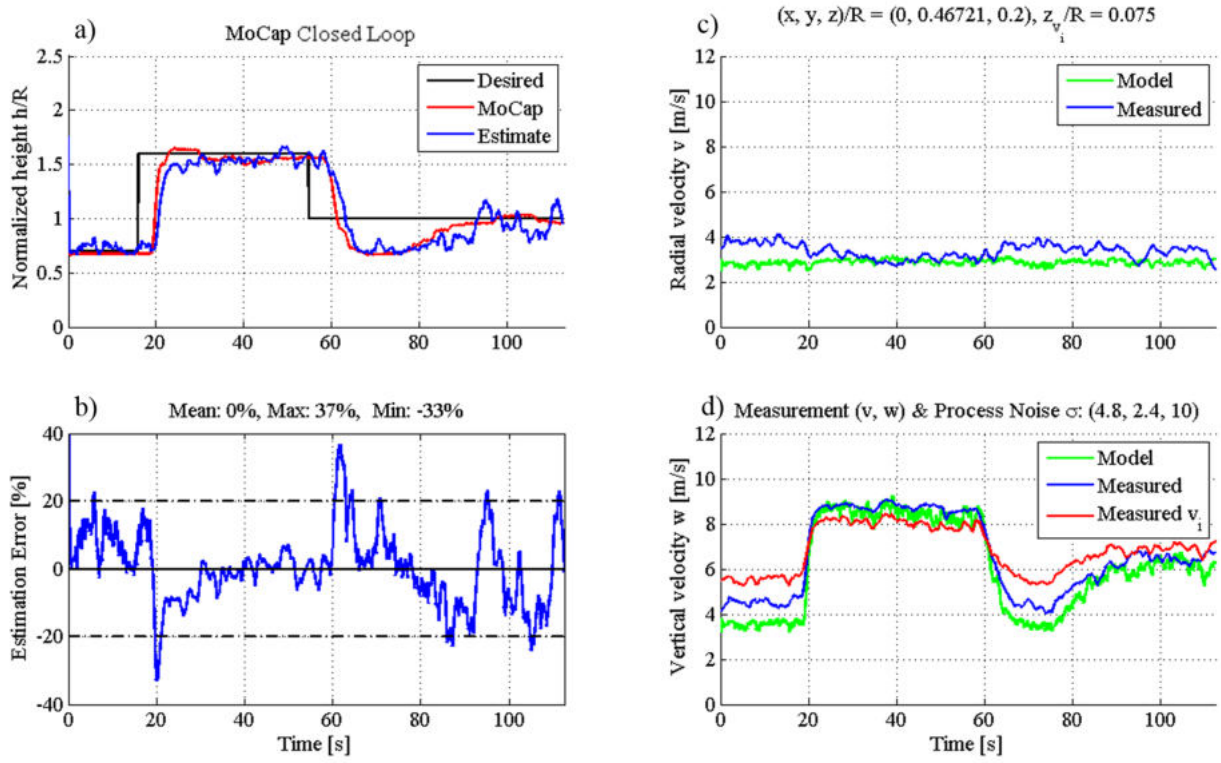

Figure 7.1: Validation of flow-sensing based Bayesian height estimation with closed-loop height tracking using motion capture. The probes are located at $(x, y) = (0, 0.4672R)$, $z/R = 0.20$ and $z_{v_i}/R = 0.075$. The standard deviation for measurement (v, w) and process noise are (4.8, 2.4, 10), $J = 50$ points for the MAF and $\delta = 500$ for quadratic smoothing. (a) Desired (black), actual(red) and estimated (blue) normalized height h/R; (b) percentage estimation error; (c) flow model (green) and measured (blue) radial velocity v; (d)flow model (green) and measured (blue) vertical velocity w and measured induced velocity v_i (red).

height changes well. Fig. 7.1(b) shows the percentage estimation error between the estimated and actual height, with zero mean error in this sample run. The mean estimation errors observed over multiple runs were less than 5% (1.1 cm or 0.44in.). Most estimation errors were within the $\pm$ 20% range. As the system settled towards a steady-state height or the system speed is sufficiently slow, the estimation quickly converged as can be seen at 30s and 65s.

Fig. 7.1(c) shows the measured (blue) and model (green) radial v velocity.

Fig. 7.1(d) shows the measured (blue) and model (green) vertical w velocity as well as the induced velocity v_i. The model velocity components plotted are the components corresponding to the estimated height with the induced velocity as input. Note that the estimation error is smallest when the model velocities match the measured velocities, which allows the Bayesian filter to accurately evaluate the likelihood function (4.2).

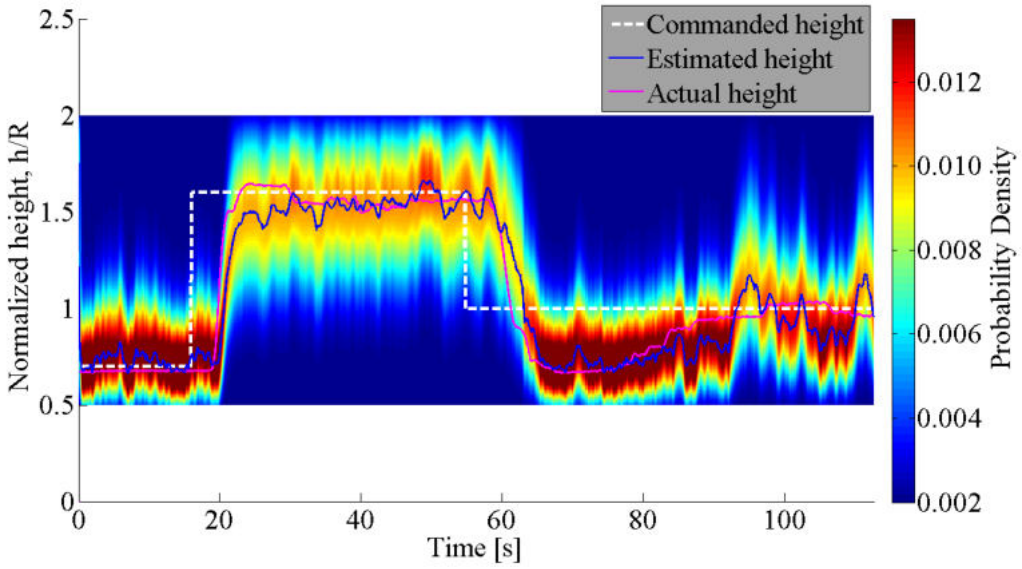

Figure 7.2: Posterior probability density of flow-sensing based Bayesian filter height estimation framework with closed-loop height tracking using motion capture.

Fig. 7.2 shows the posterior PDF of the Bayesian height estimator shown in Fig. 7.1. The axes are the same as that of Fig. 7.1 for comparison. For the first 20s when the heave stand does not move at $z/R = 0.7$, the filter is confident in its estimate, as shown by the color map. As the heave stand ascends after 20s, the filter converges quickly because the PDF has less spread. At 30s, the heave stand is making small corrections which is tracked by the filter, but it is not as confident in its estimate as it was in the first 20s, as is evident in the color map and the

large spread. However, the dynamic filter becomes more confident in its estimate from 50 – 60s because the heave stand is barely moving and the filter can make more accurate estimations based on previous measurements from a similar height. Similar performance is observed for the descent maneuver, where the filter estimate converges with the actual height from 65 – 85s.

Beyond 85s, the filter estimate bounces around and the PDF has more spread, which is likely caused by measurement noise. Note that the estimation error is the smallest within this time period at 100s, which corresponds with a match between the model and measured vertical velocity w shown in Fig. 7.1(d). Shortly before and after 100s, the velocities do not match up closely, hence the increase in estimation error. If the experimental period had been extended with the heave stand at steady-state, the dynamic filter would have been able to resolve this error, as shown in the static case of the first 20s.

7.2 Validation of Observer-based Feedback Control

The final experiment was conducted to validate the observer-based height tracking framework using only flow-sensing based Bayesian filter height estimation and feedback-feedforward control. This experiment is similar to the experiment conducted in the previous subsection, but the height for feedback control was provided by the Bayesian filter in this case. All other parameters are the same.

Fig. 7.3 shows the experimental results, which validates the Bayesian filter-based feedback-feedforward height tracking framework. Fig. 7.3(a) – (d) show the

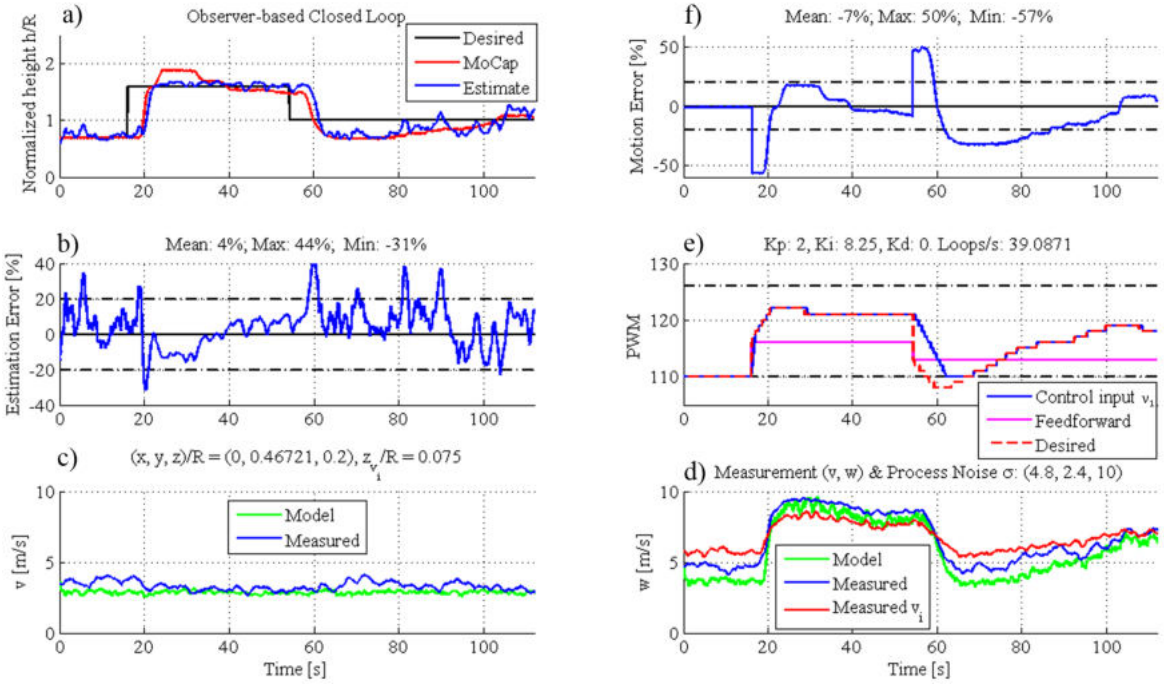

Figure 7.3: Validation of observer-based height tracking framework using only flow-sensing based Bayesian filter height estimation and feedback-feedforward control. The probes are located at $(x, y) = (0, 0.4672R)$, $z/R = 0.20$ and $z_{v_i}/R = 0.075$. The standard deviation for measurement (v, w) and process noise are (4.8, 2.4, 10), $J = 50$ points for the MAF and $\delta = 500$ for quadratic smoothing. (a) Desired (black), ground truth (red) and estimated (blue) normalized height h/R; (b) percentage estimation error; (c) flow model (green) and measured (blue) radial velocity v in m/s; (d)flow model (green) and measured (blue) vertical velocity w and measured induced velocity v_i (red) in m/s; (e) PWM control input ν_1 (blue), feedforward term (magenta), desired input (red) prior to rate limiter and saturation (dashed black). Loop speed of 39 loops/s is acheived ; (f) percentage motion error.

same plots as Fig 7.1, with the exception that this manuever is for observer-based closed-loop control. Fig. 7.3(e) shows the PWM commands for various terms, including control input ν_1 (5.10) (blue), feedfoward term (magenta) and desired control input (blue) before being rate limited and saturated between 110 – 126 PWM (dashed black). Loop speed of 39 loops/s is acheived. Fig. 7.3(f) shows the percentage motion error between desired height and actual height.

The mean estimation and motion errors for this sample case are 4% and 7%

respectively. As before, most of the estimation and motion errors fall within the ±20% range. The biggest estimation and motion errors result from changes in the commanded height around 18s and 55s. For multiple runs with the same parameters, the mean estimation errors were observed to be less than 5% (1.1 cm or 0.44in.) and the motion errors were less than 9% (2 cm or 0.79 in.). Another factor to consider when evaluating the cause of estimation errors beyond unsteady aerodynamics, tip effects and measurement and process noise is that the estimation error is close to the mean probe tip-to-tip length of 1.2 cm, which is in effect the average resolution of my probes.

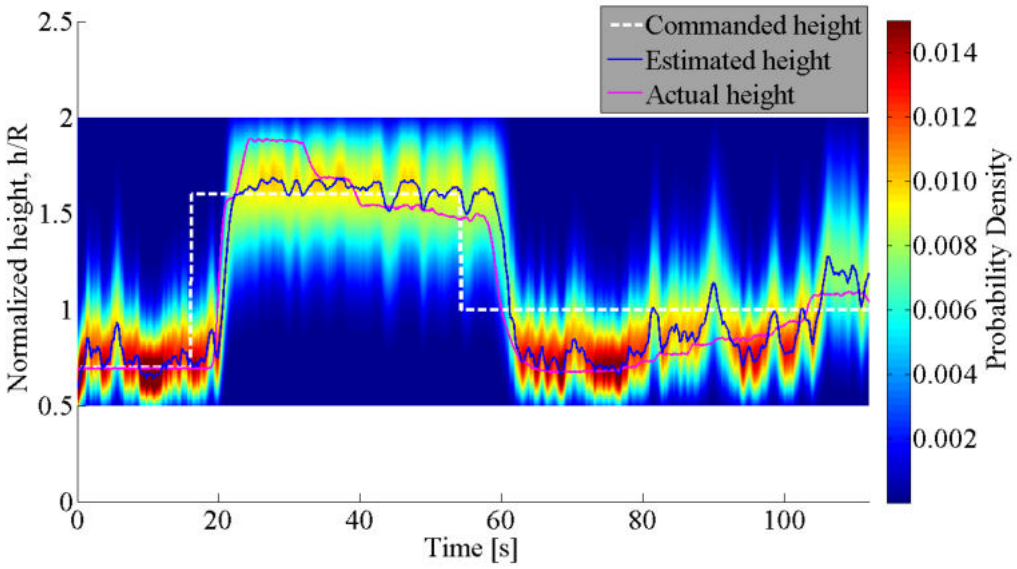

Figure 7.4: Posterior probability density of observer-based height tracking framework using only flow-sensing based Bayesian filter height estimation and feedback-feedforward control.

Fig. 7.4 shows the posterior PDF of the Bayesian height estimator used for closed-loop control, as shown in Fig. 7.3. In general, the PDF tracks height changes well and converges to the actual height quickly. Generally, the filter for observer-based closed-loop control is less certain of its estimation than that of Mo-

Cap closed-loop control, as shown by their color maps (both PDF color maps have their thresholds set at 70% of maximum probability).

From 25 – 35s, the feedback controller drives the estimated height to the commanded height, but there is a mismatch with the actual height as the filter is not estimating well at this time frame. The filter is also not as confident in its estimation, as shown by the large spread in the PDF. Note that the PDF in both observer-based and MoCap closed-loop control have large spread in their PDFs and lower probabilities at the high end of the grid, which could be caused by weaker ground effect at greater heights. Once again, as the system settles into steady-state height at 40s and 105s, the filter converges to the actual height and the closed-loop control is capable of driving the system to the right height.

Chapter 8: Conclusions

This thesis describes a framework for dynamic height estimation and observer-based feedback control using flow sensing for rotorcraft operation in ground effect. A ring-source flow model for the rotor downwash in ground effect developed using potential flow theory captures the essential characteristics of the relationship between flow velocity and height. The reduced-order flow model used for fast evaluation of the flowfield in a recursive control loop has been experimentally validated. It was found that the flow model best predicts the flowfield with measurements collected mid-radius. A ring-source potential flow model with tilt to introduce roll or pitch angle is also developed. A static and a dynamic compound pendulum heave test stand were built and their merits are discussed. A nonlinear dynamic model of the compound pendulum heave test stand which reduces to the dynamics of a rotorcraft landing in ground effect is derived and allows for the study of the open-loop dynamics and facilitates the design of a closed-loop controller. It is shown that a uniform sideward wind increases the thrust of a rotor in ground effect and does not cause instability. A uniform axial wind from the top of the rotor can cause instability, if it has greater magnitude than the rotor induced velocity. The height of the rotorcraft in ground effect is experimentally estimated with a grid-based recur-

sive Bayesian filter using the three-dimensional flow model and differential pressure probe measurements. Finally, flow-estimation-based closed-loop control is implemented, demonstrating that height estimation and control is possible using only flow sensing and modeling. Mean estimation error no greater than 5% (1.1 cm or 0.44 in.) and mean motion error no greater than 9% (2 cm or 0.79 in.) is achievable.

Bibliography

[1] Tritschler, J., "Contributions to the Characterization and Mitigation of Rotorcraft Brownout," Doctor of Philosophy Dissertation, Department of Aerospace Engineering, University of Maryland, 2012.

[2] Plank, V.G., Spatola, A.A., Hicks, J.R., "Fog Modification by Use of Helicopters," Air Force Cambridge Research Laboratories, U.S. Army Atmospheric Sciences Laboratory, AFCRL-70-0593, Environmental Research Papers No. 335, ECOM-5339, October 28, 1970.

[3] Serra, P., Cunha, R., Silvestre, C., "On the Design of Rotorcraft Landing Controllers," 16th Mediterranean Conference on Control and Automation Ajaccio, France, June 25-27, 2008.

[4] Mahony, R., Hamel, T., "Adaptive Compensation of Aerodynamic Effects during Takeoff and Landing Manoeuvres for a Scale Model Autonomous Helicopter," *European Journal of Control*, (2001)0:1-15, 2001.

[5] Nonaka, K., Sugizaki, H., "Integral Sliding Mode Altitude Control for a Small Model Helicopter with Ground Effect Compensation," American Control Conference, San Francisco, CA, June 29 - July 01, 2011.

[6] Borenstein, J., Koren, Y., "Obstacle Avoidance with Ultrasonic Sensors," *IEEE Journal for Robotics and Automation*, Vol. 4, No. 2, April 1988.

[7] Tanigawa, M., Luinge, H., Schipper, L., Slycke, P., "Drift-Free Dynamic Height Sensor using MEMS IMU Aided by MEMS Pressure Sensor," Proceedings of the 5th Workshop on Positioning, Navigation and Communication, 2008.

[8] Prouty, R.W., *Helicopter Performance, Stability, and Control*, Krieger Publishing Company, Florida, 2002.

[9] Govindarajan, B., "Evaluation of Particle Clustering Algorithms in the Prediction of Brownout Dust Clouds," Master's Thesis, Department of Aerospace Engineering, University of Maryland, August 2011.

[10] Cheeseman, I.C., Bennett, W.E., "The Effect of the Ground on a Helicopter Rotor in Forward Flight," Reports & Memoranda No. 3021, Ministry of Supply, Aeronautical Research Council Reports and Memoranda, September 1955.

[11] Yeo, D. W., Sydney, N., Paley, D., Sofge, D., "Onboard Flow Sensing For Downwash Detection and Avoidance On Small Quadrotor Helicopters," AIAA Guidance, Navigation and Control Conference 2015, accepted for publication.

[12] Lagor, F.D., DeVries, L.D., Waychoff, K., Paley, D.A., "Bio-inspired Flow Sensing and Control: Autonomous Rheotaxis Using Distributed Pressure Measurements," *Journal of Unmanned System Technology*, Nov 2013.

[13] DeVries, L.D., Lagor, F.D., Lei, H., Tan, X. ,Paley, D.A., "Distributed Flow Estimation and Closed-Loop Control of an Underwater Vehicle with a Multi-Modal Artificial Lateral Line," *Bioinspiration & Biomimetics*, special issue on "Hybrid and Multi-modal Locomotion," accepted for publication.

[14] Hooi, C.G., Lagor, F. , Paley, D., "Flow Sensing, Estimation and Control for Rotorcraft in Ground Effect," IEEE Aerospace Conference, Big Sky, Montana, March 2015.

[15] Hooi, C.G., "Design, Rapid Prototyping and Testing of a Ducted Fan Microscale Quadcopter," 70th American Helicopter Society Society Annual Forum & Technology Display, Montreal, Quebec, Canada, May 2014.

[16] Hooi, C.G., Lagor, F. , Paley, D., "Flow Sensing, Estimation and Control for Rotorcraft in Ground Effect: Modeling and Experimental Results, " 71st American Helicopter Society Society Annual Forum, Virginia Beach, VA, May 2015.

[17] Lee, T.E., Leishman, J.G., Ramasamy, M., "Fluid Dynamics of Interacting Blade Tip Vortices with a Ground Plane," *Journal of the American Helicopter Society* 55, 022005, 2010.

[18] Leishman, J.G., *Principles of Helicopter Aerodynamics*, 2nd. Ed., p.258 - 260, Cambridge University Press, New York, 2006.

[19] Hess, J.L., Smith, A.M.O., "Calculation of Potential Flow about Arbitrary Bodies," *Progress in Aerospace Sciences*, Volume 8, p. 39–40, 1967.

[20] Bangura, M., Lim, H., Kim, H.,J., Mahony, R., "Aerodynamic Power Control for Multirotor Aerial Vehicles," 2014 IEEE International Conference on Robotics & Automation (ICRA), Hong Kong, China, May 2014.

[21] Bangura, M., Mahony, R., "Nonlinear Dynamic Modeling for High Performance Control of a Quadrotor," Proceedings of Australasian Conference on Robotics and Automation, New Zealand, December 2012.

[22] Leishman, R.,C., MacDonaLd Jr., J.,C., Beard, R., W., McLain, T., W., "Quadrotors and Accelerometers: State estimation with an improved dynamic model," IEEE Control Systems Magazine, February 2014.

[23] Murphy, K., *Machine Learning: A Probabilistic Perspective*, The MIT Press, Cambridge, Massachusetts, London, 2012.

[24] Simon, D., *Optimal State Estimation: Kalman, H Infinity, and Nonlinear Approaches* , 1st. Ed., p.465-466, John Wiley & Sons, Inc., New Jersey, 2006.

[25] Arulampalam, M.S., Maskell, S., Gordon, N., Clapp, T., "A Tutorial on Particle Filters for Online Nonlinear/Non-Gaussian Bayesian Tracking," *IEEE Transactions on Signal Processing*, Vol. 50, No. 2, February 2002.

[26] Julier, S., Uhlmann, J., "Unscented Filtering and Nonlinear Estimation", *Proceedings of the IEEE*, Vol. 92, No. 3, March 2004.

[27] Gillijns, S., Barrero Mendoza, O., Chandrasekar, J., De Moor, B. L. R., Bernstein, D. S., Ridley, A., "What Is the Ensemble Kalman Filter and How Well Does it Work?", Proceedings of the 2006 American Control Conference Minneapolis, Minnesota, USA, June 14-16, 2006.

[28] Boyd, S., Vandenberghe, L., *Convex Optimization*, p.312, Cambridge University Press, 2014.

[29] Skogestad, S., Postlethwaite, I., *Multivariable Feedback Control, Analysis and Design*, 2nd. Ed., John Wiley and Sons.